MÖSSBAUER STUDY OF SYNTHETIC HEMATITE AGGREGATES

by

Mei-Zhen Dang

Thesis Submitted to

the School of Graduate Studies and Research

in partial fulfilment of the requirements for the degree

of Master of Science in Physics

Physics Department

Faculty of Science

University of Ottawa

Ottawa, Canada

ISBN 0-315-85840-0

Canada

UNIVERSITÉ D'OTTAWA
UNIVERSITY OF OTTAWA

ABSTRACT

Synthetic hematite aggregates that result from a process that may have industrial and environmental relevance are studied by Mössbauer spectroscopy at room temperature and liquid nitrogen temperature. The Mössbauer results are compared to measurements involving chemical analysis, scanning electron microscopy, and X-ray diffraction on the same samples. Factors such as the crystalline quality of the hematite and the overall sample purity (wt%Fe_2O_3) are followed as functions of the known synthesis conditions. Pure bulk hematite (high quality α-Fe_2O_3) serves as a reference throughout. Mössbauer spectroscopy is useful in two ways in this problem: (i) it can detect and identify iron-bearing impurities (i.e. non-hematite Fe-compounds), and (ii) it gives much detailed microscopic information on the intra-sample hematite.

We find that all of the sulphur seen by chemical analysis probably resides in an iron-bearing compound which, most often, is probably a quenstetite-like material: $Fe_2(SO_4)_3.nH_2O$ (n = 9-11). The synthesis conditions are understood to determine both the hematite yield (or sample purity: wt%Fe_2O_3) and the intra-hematite crystalline quality, in that these two factors are correlated. Our interpretation of the room temperature Mössbauer spectra

resolves coexisting bulk-like and high-defect-density regions whose relative amounts and sample-dependent Mössbauer characteristics can be quantified accurately.

On going to liquid nitrogen temperature, a Morin transition is seen to have occurred in all regions of the most bulk-like samples, to have occurred in some regions of intermediate samples, or not to have occurred at all in the samples with the highest defect-density hematites. This illustrates the intricate interplay between microstructural details and cooperative magnetism in hematite materials.

ACKNOWLEDGEMENTS

First of all, I wish to express my sincere thanks to my supervisor Dr. D.G. Rancourt for giving me the opportunity to work with him and for his invaluable guidance, support, and encouragement throughout the course of this work.

Also I want to thank Dr. J.E. Dutrizac at CANMET for supplying samples and SEM pictures.

Thanks to Dr. R. Provencher for doing room temperature Mössbauer measurements of the L samples.

Thanks to Dr. H. Kodama at Agriculture Canada for performing the X-ray diffraction for our samples.

Thanks to Dr. G. Lamarche for performing SQUID magnetic measurements on our samples.

Thanks to Riccardo Brun Del Re and Mike Royer for help on X-ray diffraction analysis and experimental technique.

Thanks to all my friends who have given me help on this work.

Finally I want to thank my family for their moral support.

ABBREVIATIONS AND SYMBOLS

AF	Anti Ferromagnetic (state)
BG	BACKGROUND
CS	Center Shift
efg	electric field gradient
FWHM	Full Width at half maximum (of absorption line)
HFD	Hyperfine Field Distribution
HFD'S	Hyperfine Field Distributions
JCPDS	Joint Committee on Powder Diffraction Standards
LT	Low temperature (LT ≃ 80K in this work)
LP	Line position
PBH	Pure Bulk Hematite
QS	Quadrupole splitting
R1	Ratio of line intensity for line-1/line-3
R2	Ratio of line intensity for line-2/line-3
RT	Room temperature (RT ≃ 296 K)
SQUID	Superconducting Quantum Interference Device
T_M	Morin transition temperature
T_N	Neel temperature
SEM	Scanning Electron Microscopy
WF	Weak Ferromagnetic
XRD	X-Ray Diffraction

Ai/A_t	Spectral area ratio for the ith HFD component to the total spectral area
δ_0	CS without coupling to hyperfine field
δ	total CS of an elemental spectrum
δ_1	coupling parameter of δ to distributed hyperfine field (H or z)
$\sim$	electronic charge
ε_0	QS without coupling to hyperfine field

ε	QS in coupling to hyperfine field
ε_1	coupling parameter of the QS to H or z
E_d	magnetic dipolar and pseudo-dipolar anisotropy energy
E_{cry}	magnetic single ion anisotropy energy
G(x,a)	Gaussian distribution function
g	nuclear g-factor for ground state of Fe-57
g*	nuclear g-factor for the first exited state of Fe-57
hi	Lorentzian height for ith line
H	Hyperfine magnetic field and spin Hamiltonian
I,I*	ground state and first exited state Fe-57 nuclear spin quantum number
γ	Lorentzian line FWHM
L(a;x)	Lorentzian function; a is the parameter and x is the variable
θ,ϕ	polar angle between hyperfine field and efg principal axis
p_i	weight factor for ith Gaussian component in a hyperfine field distribution
q	electric field gradient at nucleus in principal axis direction
Q	nuclear electric quadrupole moment
η	asymmetry parameter
σ_i	Gaussian HFD width for the ith component
μ_i	magnetic moment for the specific sites
μ_B	Bohr magneton
μ_N	nuclear magneton
V(a;x)	Voigt function; a is the parameter, x is the variabl
z	Zeeman hyperfine splitting
z_0	center cf the Gaussian component of a z-distribution

LIST OF FIGURES

LIST OF TABLES

TABLE OF CONTENTS

1. INTRODUCTION

In this thesis, we have used Mössbauer spectroscopy and other techniques to find out the most we could about certain synthetic hematite products that have relevance to industry.

Iron is one of the most common elemental constituents of the Earth's crust. Many industrial purification processes of ores give rise to large quantities of iron-bearing residues as unwanted by-products. Many such products are environmentally suspect and must be impounded in large piles, where leakage to the environment is of constant concern.

Consider the manufacturing of metallic zinc. Most zinc concentrates contain several percent of iron. This iron is first dissolved and then precipitated into a filterable form. The rejected iron compound is often a jarosite-type compound $MFe_3(SO)_2(OH)_6$, where M = Na, NH_4, K, H_3, Ag, etc.

Rather than stock these iron compounds into large piles, one approach is to convert them into hematite (α-Fe_2O_3). This results in lower volumes of the chemically very stable iron oxide. In addition, pure hematite is a commercially valuable iron ore.

Researchers at CANMET (Dutrizac 1989) have studied the conversion of jarosite-type compounds into hematite. The resultant nominal hematite always contains 1-7% SO_4 impurity

— an unacceptable impurity level in view of iron production. Also the exact chemical nature of the sulphur and its relation to the hematite are unknown. Various experimental methods have been unable to elucidate how the SO_4 is incorporated into the "hematite" material. For example, X-ray diffraction often only indicates the presence of well crystallized hematite.

Mössbauer spectroscopy has proved to be a very useful tool in materials science. It gives an enormous amount of information that serves in compound identification and characterization. By computer analysis, it gives detailed chemical (e.g. valence state of Fe), crystallographic (e.g. local defects and distortions) and microstructural (e.g. superparamagnetism) information. In fact, even preliminary tests showed distinctive differences in the room temperature Mössbauer spectra of several of the CANMET products. In particular, line broadening was found to increase with increasing known SO_4 content.

In cooperation with CANMET, we have performed an in-depth Mössbauer study of the hematite products. Mössbauer spectra were collected at room temperature and liquid nitrogen temperature. For the first time, we apply a new recently developed hyperfine field distribution method to analyze synthetic hematite materials having gradual variations in impurity amounts and crystalline quality.

Many physical properties were found to be correlated to the overall sample purity (wt% Fe_2O_3), or inversely to the total amount of impurity (100 - wt% Fe_2O_3). By using Mössbauer spectroscopy in conjunction with X-ray diffraction, chemical elemental analysis, and scanning electron microscopy, we have characterized the impurities and the hematite as fully as possible with these methods.

In trying to extract as much information as possible from our spectra collected at different temperatures, we have had to determine which spectral analysis methods and models are best suited to our problem. In this process, we have developed how to use the Mössbauer spectroscopy technique effectively in this and similar problems.

In addition, all work on hematite materials contributes to our general understanding of a unique magnetic phenomenon that occurs in these materials: the Morin transition (Morin 1950). In pure bulk α-Fe_2O_3, this transition is a relative sharp cooperative spin flop transition occurring at $T_M \simeq 250$ K (depending on the origin of the particular sample). In other synthetic and natural hematites, the Morin transition is sensitive to particle size, lattice defects, and foreign elements. It is known that small particle size, poor crystal quality and most impurities all suppress the Morin transition by first lowering T_M and broadening the transition. Understanding how each of these affects the

Morin transition is of ongoing fundamental interest.

With our impurity containing hematites, we systematically investigated how the Morin transition changes with overall sample purity and hematite crystalline quality. This is the first study on such a broad range of hematites that have been synthesized under similar conditions. It is of both fundamental and practical significance.

2. BACKGROUND

2.1 Structure of Hematite

Hematite has a rhombohedral structure with space group D^6_{3d}(or $R\bar{3}c$). Its lattice parameters are a = 5.42 Å and α = 55°17′. The [111] axis is the 3-fold symmetry axis, and (111) is the basal plane.

For convenience, it is often indexed in the hexagonal system since the oxide comprises hexagonally close-packed planes of oxygens stacked along the [111] axis (Fig.2.1.1(a)) with Fe^{3+} cations occupying only two-third of the octahedral sites (Fig.2.1.1(b)). On a given anion layer, the arrangement of the cations is shown in Fig.2.1.1(c).

Fig.2.1.2 shows the rhombohedral unit cell and its relation to the stacking of hexagonal layers. On the different adjacent layers, the positions of the cations shift regularly, see Fig.2.1.3.

Each FeO_6 octahedron contains three shared and three unshared edges not in the basal plane, and one shared plus one unshared face in the basal and/or top planes, respectively. The octahedra are considerably distorted with the oxygen-oxygen distances along the shared edges and shared basal face being considerably shorter than those

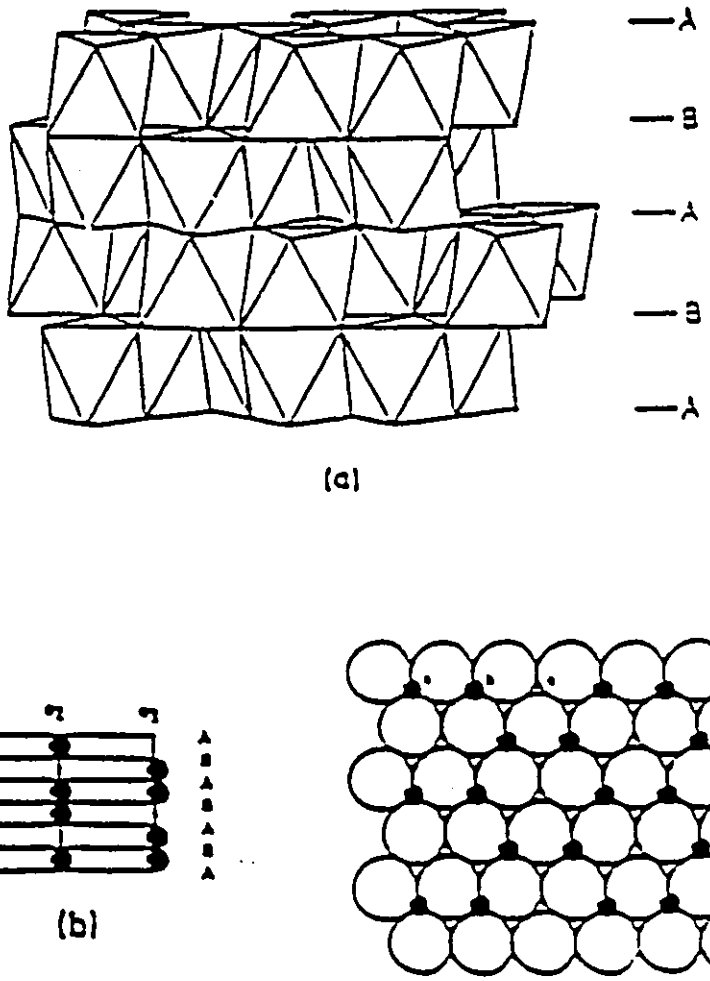

Fig.2.1.1 (a) Hematite layering of octahedra. Each octahedron has a central Fe^{3+} cation and 6 O^{2-} anions on its corners. (b) Cation distribution scheme on stacked anion layers with Fe^{3+} occupying only two-third of the octahedral sites. (c) Arrangement of cations on a given anion layer.

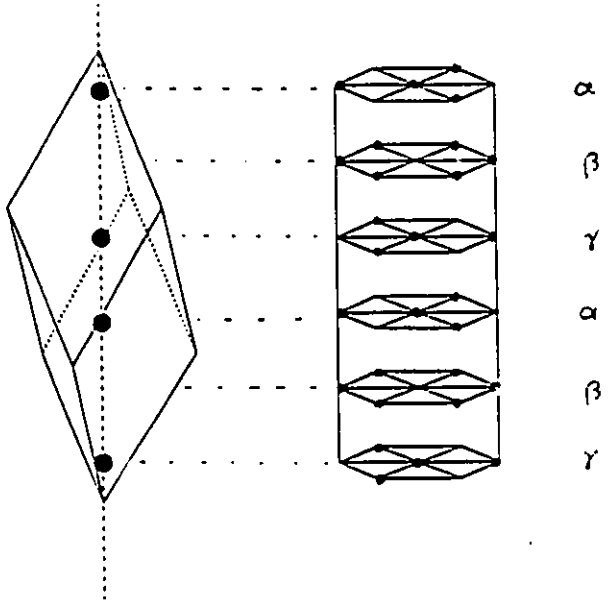

Fig.2.1.2 Hematite rhmobohedral unit cell (left) and its relation to the stacking of hexagonal planes of Fe^{3+} (right).

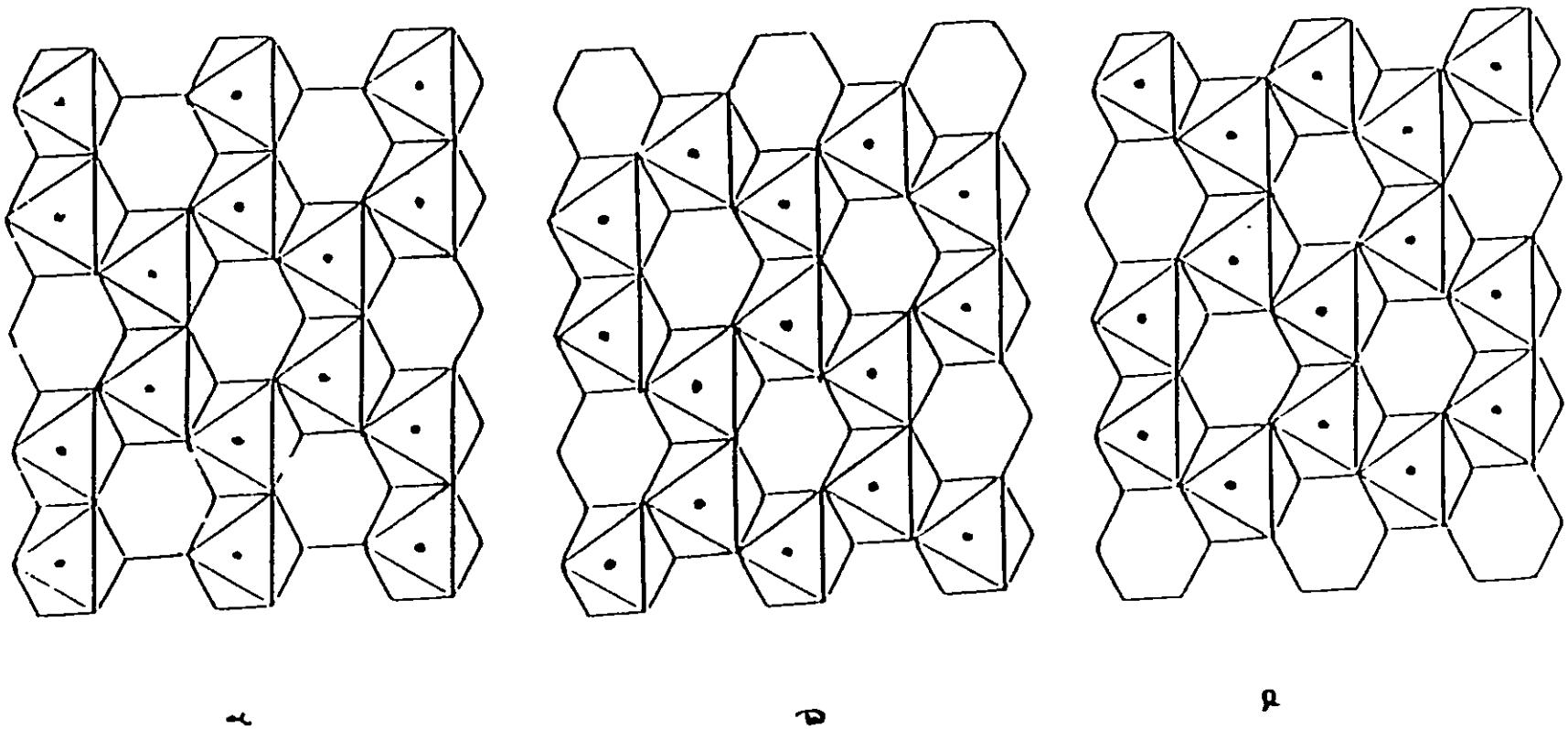

Fig.2.1.3 Projectiors on the (111) plane, of stacked octahedral layers. On adjacent layers, positions of the cations shift regularly (compare to Figs.2.1.1 and 2.1.2).

along the unshared edges and unshared basal face. The iron atoms lie closer to the unshared faces of the octahedra than to the shared faces.

2.2 The Magnetic Structure of Pure Bulk Hematite and the Morin Transition

The Magnetic structure of hematite was determined by neutron diffraction (Shull et al, 1951). Between the Neel temperature (T_N ~ 948 K to 963 K) and the Morin temperature ($T_M \simeq 250$ K), hematite is in a weak ferromagnetic (WF) state, in which all moments lie approximately in the (111) plane with a small canting out of the plane giving a small net average magnetic moment per Fe atom. Below T_M, hematite is in an antiferromagnetic (AF) state and all spins are aligned in the [111] direction and are truly antiparallel. Fig 2.2.1 illustrates the WF state (left) and the AF state (right) in pure bulk hematite.

The Morin transition is a temperature driven collective spin flip occurring between the high temperature WF state and the low temperature AF state. "Weak ferromagnetism" means that certain predominantly antiferromagnetic crystals such as α-Fe_2O_3 exhibit spontaneous magnetization due to

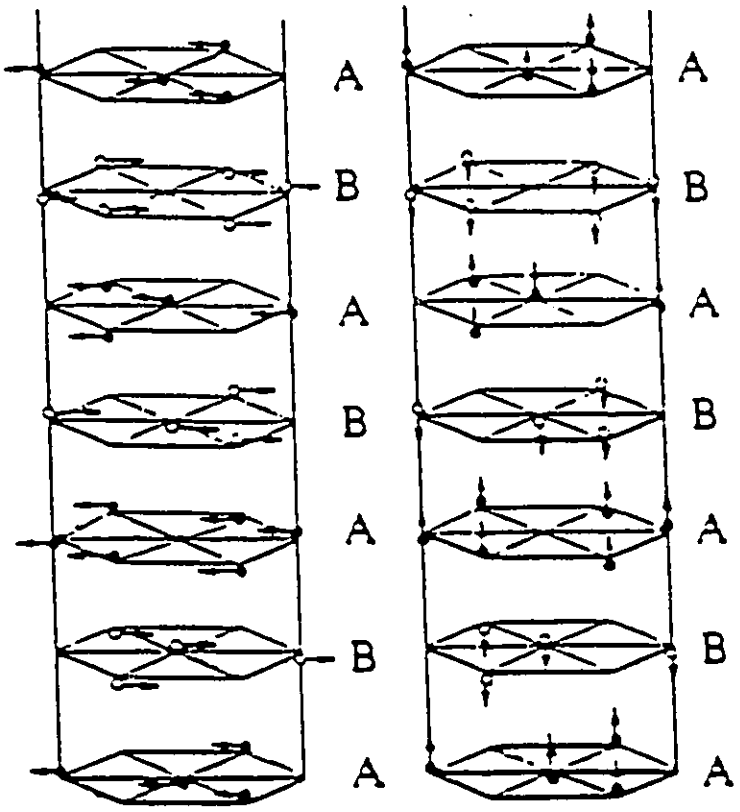

Fig.2.2.1 The two magnetic state spin structures of hematite: the WF state (left), and the AF state (right).

spin canting. The magnitude of the average net magnetic moment per atom is extremely small. It usually varies between the limits of 10^{-2} - 10^{-5} of the sublattice value. According to Dzyaloshinsky (1958) and Moriya (1960), the canting is an intrinsic property arising from an anisotropic exchange interaction.

Theoretically the Morin transition can be described by a spin Hamiltonian for α-Fe_2O_3 (Van de Woude 1966):

$$H = \sum_{j,k} \{J_{jk}(S_j \cdot S_k) + d_{jk} \cdot [S_j \times S_k] + S_j \cdot K_{jk} S_k\} + \sum_j \{D S_{jz}^2 + \mu_B S_j g_j \cdot H\} \qquad (2.2.1)$$

where the first term in the first sum is the superexchange interaction, the second is the antisymmetrical spin coupling, the third represents the magnetic dipolar and pseudo-dipolar (E_d) anisotropy energy. In the second sum, the first and second terms are the single ion anisotropy (E_{cry}) and Zeeman energies, respectively.

E_d favors the (111) plane. E_{cry} has the opposite sign and favors the [111] axis direction. Both are related to the temperature, and compete to decide the spin orientation. The antisymmetric term is responsible for the canting or weak ferromagnetism.

At RT, E_d dominates over E_{cry}, and spins lie in the

(111) direction with the small canting. The spins stay in this WF state. When the temperature is lowered below T_M, the E_{cry} term becomes larger than the E_d term, then the spin reorientation takes place. At this temperature spins flip to the [111] direction and stay in the pure antiferromagnetic state at lower temperatures. The state change from WF state to AF state is the Morin transition. In pure bulk hematite it is usually argued to be a first order transition. However, this is still one of many open questions.

2.3 Mössbauer Spectroscopy Background

An interaction between a nucleus and its surrounding electrons (and hence its chemical and physical environment) is called a hyperfine interaction. There are three kinds of such interactions Which can be studied by Fe-57 Mössbauer spectroscopy. They are the electric monopole (i.e. Coulombic) interaction, the electric quadrupole interaction and the magnetic dipole interaction.

In the spectra, these interactions manifest themselves respectively as an isomer shift, a quadrupole splitting and a hyperfine splitting. These, in turn, are parameterized by

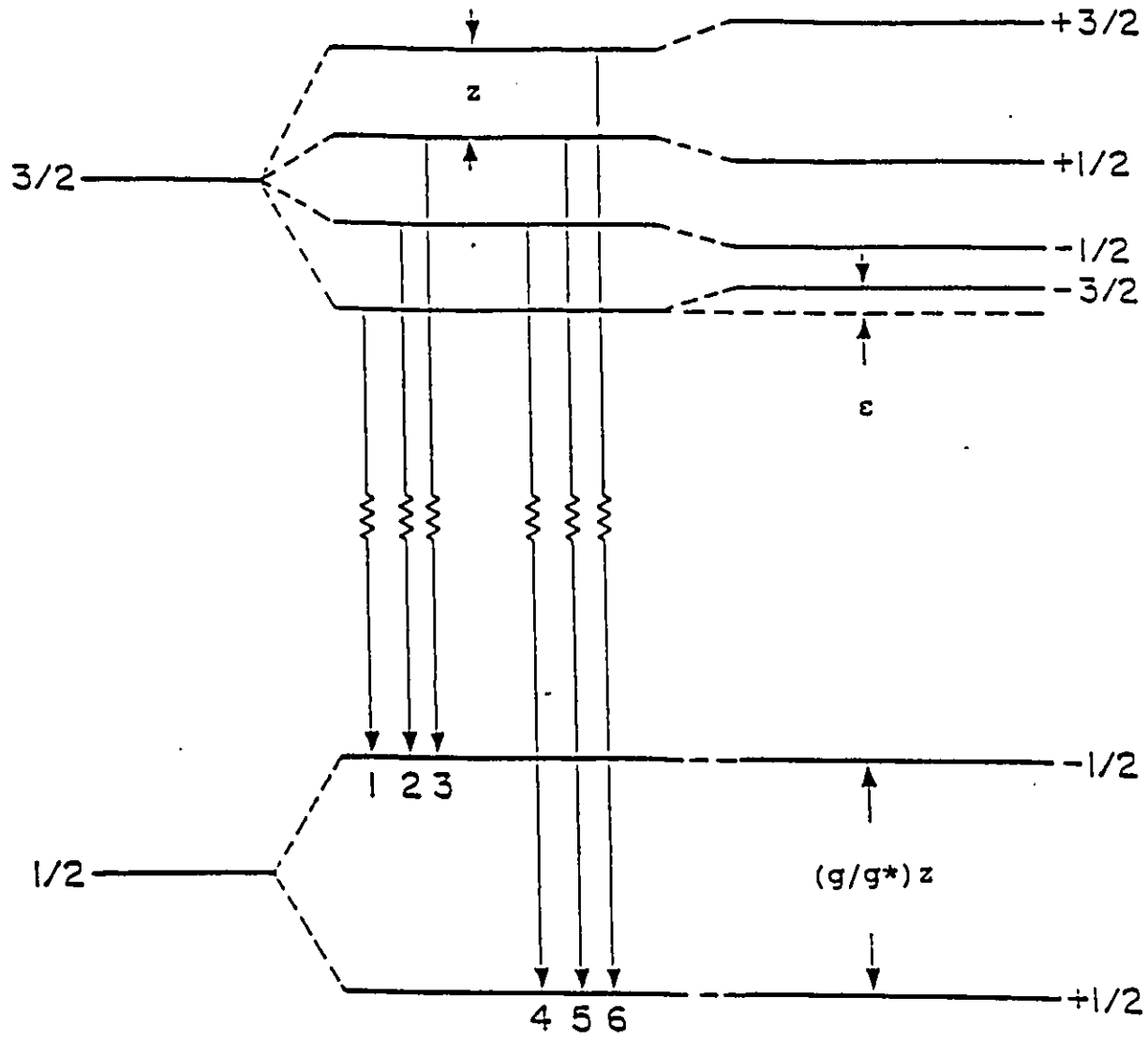

Fig 2.3.1 Iron-57 nuclear energy levels: first in presence of a magnetic field only and then with the additional presence of a small quadrupole interaction.

the center shift (CS=δ) with respect to some standard absorber and including both the isomer shift and the second order Doppler shift, the electric quadrupole splitting ε and the hyperfine magnetic Zeeman splitting (z). The relevant energy splittings and shifts are shown in Fig.2.3.1.

A particular environment is often referred to as a site. Microscopically, one specific site is characterized by a particular set of hyperfine interaction parameters in Mössbauer spectroscopy.

When a probe nucleus (^{57}Fe in our case) is in a particular effectively static electric or chemical environment and under ideal experimental conditions, the Mössbauer spectrum is strictly Lorentzian (i.e. composed of Lorentzian absorption lines). In real samples, however, even for a single site material, there are inhomogeneities of various types, which make the actual environments spread in a certain range. The hyperfine fields may, in a first approximation, lead to Gaussian distributions of Lorentzian line positions. The line shape is then a convolution of a Gaussian with a Lorentzian, called a Voigt line, and is expressed as:

$$V(\omega_o,\sigma,\gamma,h_L;\omega) = \int_{-\infty}^{\infty} L(\gamma,h_L,x;\omega)\ G(\sigma,\omega_o;x)\ dx \qquad (2.3.1)$$

where

$$L(\gamma,h_L,x;\omega) = \frac{\gamma^2 h_L/4}{(\omega-x)^2+\gamma^2/4} \qquad (2.3.2)$$

is an elemental Lorentzian with height h_L, FWHM γ, and centered on x and

$$G(\sigma,\omega_o;x) = \frac{1}{\sqrt{2}\,\sigma} \exp(-(x-\omega_o)^2/2\sigma^2) \qquad (2.3.3)$$

is a normalized Gaussian distribution function with standard deviation σ, x is the distribution variable, and ω_o is the center value of the distribution.

The Voigt profile does not have an exact analytic closed form expression. But an excellent analytic approximation has been developed (Martin et al.,1981) that makes fitting applications possible and practical.

2.4 Physical Origin of Hyperfine Field and its Distribution

According to Ping and Rancourt (1992) and Panissod et al. (1982) and Johnson et al. (1963), the average hyperfine field for a given site is the vector sum of a local term and a transferred term. The hyperfine field magnitude for the ith site can therefore be written as:

$$|H_i| = | A \langle \mu_i \rangle + \sum_{j,nn} B^{ij} \langle \mu_j \rangle | \qquad (2.4.1)$$

The first term on the right hand side is proportional to the magnetic moment of the iron on the site itself. It is the local term. The second term is a vector sum over all magnetic moments of the near neighbors and is the transferred term (the transferred term may also include smaller next-near-neighbor contributions).

With Eq.2.4.1 we can see that the magnitude of the hyperfine field for a given site depends on both the on-site moment, the moments of its neighbors, and the spatial configurations of its near neighbors as well.

In a real "single-site" material, the environments for all the sites may not be exactly the same, the hyperfine field magnitudes will then of course be slightly different. When the environments for all the irons spread in a certain range, this will lead to continuous hyperfine field distributions.

2.5 Hyperfine Field Distribution Program

Rancourt and Ping have developed a powerful approach to deal with arbitrary-shape hyperfine field distributions (HFD) (Rancourt and Ping, 1991). The distribution is written as :

$$P(z) = \sum_{i=1}^{N} P_i \quad G_i(z_{0i}, \sigma_{zi}; z) \qquad (2.5.1)$$

where N is the total number of Gaussian distribution components being used. For the ith component of the HFD, P_i is the weighting factor, σ_{zi} is the standard deviation, z_{0i} is the center value and $z = g^*\mu_N H$ is the hyperfine Zeeman splitting of the excited state. The HFD's are taken to be sums of Gaussian components, and corresponding spectra are sums of Voigt lines.

In this HFD program, some parameters are used to describe the three hyperfine interactions (section 2.3) in terms of the HFD. For a specific site, we have specific values of the parameters δ, ε, and z, whose physical meanings have been represented clearly in Fig.2.3.1. In addition, there are parameters for the height (or depth) of line-3 and for the height ratios of line-1/line-3 and of line-2/line-3. There are also couplings of center shift

and quadrupole splitting to the distributed hyperfine field as:

$$\delta = \delta_o + \delta_1 z \qquad (2.5.2)$$

$$\varepsilon = \varepsilon_o + \varepsilon_1 z \qquad (2.5.3)$$

where, δ_1 is the coupling parameter between center shift (δ) to hyperfine field (z or H) and ε_1 is the coupling parameter between quadrupole shift ε to the distributed field. In this case, both the center shift and the quadrupole splitting will also have distributions as long as z (or H) has.

Therefore, a particular group or family of sites has a HFD and particular coupling parameters to δ and ε. Such a group or family of crystallographic sites will be referred to as a (generalized) "site". In this way, a "1-site/2-component fitting model" is a fitting model in which we assume a single such "site" having two Gaussian components (N=2 in Eq.2.5.1) in its HFD, etc.

3. SAMPLE CHARACTERIZATION

3.1. Chemistry of the Synthetic Hematites

Samples studied in this work are powders of synthetic hematite aggregates. They were supplied by Dr. Dutrizac at CANMET.

The general hematites of interest are products resulting from jarosite-type compounds to hematite conversion. The method of synthesis, by which jarosite compounds $MFe_3(SO_2)(OH)_6$ (where M = Na, NH, K, HO_3, Ag, 1/2 Pb^{2+}, etc.) are converted into hematite by hydrothermal reaction at temperature T > 200 ^{0}C, is described by Dutrizac (1989). The reaction involves an initial decomposition of the jarosite, followed by the precipitation of hematite from the resulting acid ferric sulphate solution. The overall reaction sequence is:

$$2\ MFe_3(SO_4)_2(OH)_6 + 6\ H_2SO_4 \rightarrow 3\ Fe_2(SO_4)_3 + M_2SO_4 + 12\ H_2O \qquad (3.1.1)$$

$$3\ Fe_2(SO_4)_3 + 9\ H_2O \rightarrow 3\ Fe_2O_3 + 9\ H_2SO_4 \qquad (3.1.2)$$

The syntheses for our particular samples were performed in two different ways.

(i) Hematite precipitation by direct oxidation of

ferrous sulphate solutions by the reaction:

$$4\ FeSO_4 + 3\ O_2 \rightarrow 4\ SO_4 + 2\ Fe_2O_3 \qquad (3.1.3)$$

produced the samples L1, L3, L7, L9 and L10. These samples will be referred to as the "L samples".

(ii) Hematite precipitation from ferric sulphate solutions starting directly from Eq.(3.1.2) was used for samples G12, G1 and M60. These samples, along with L9, will be referred to the "Ottawa samples" because only this group was studied in detail at University of Ottawa.

The synthesis details are given in Table 3.1.1. The reactions were carried out in a batch mode. The contents were heated to certain temperatures, held at temperature for an appropriate time, and then cooled to room temperature. When cooled, the precipitates were filtered, washed and dried at 110 °C overnight, and then the products were analyzed.

In this work, only the Ottawa samples (G12, G1, M60 and L9) were studied in detail (room temperature and liquid nitrogen temperature Mössbauer spectroscopy, powder XRD on an automated diffractometer, SEM pictures of both polished section and loose powder mounts, and Debye-Sherrer and Guinier XRD). Samples L1, L3, L7 and L10 were studied only at CANMET by room temperature Mössbauer spectroscopy and

Table 3.1.1. Synthesis conditions†

Sample	solution	seed	temperature	time	pressure
L1	$FeSO_4$	no	160 °C	2 h	100 psi O_2
L3	$FeSO_4$	no	180 °C	2 h	100 psi O_2
L7	$FeSO_4$	no	220 °C	2 h	100 psi O_2
L9	$FeSO_4$	no	240 °C	2 h	100 psi O_2
L10	$FeSO_4$	no	250 °C	2 h	100 psi O_2
G1	0.5 M* $Fe(SO_4)_{1.5}$ 0.05 M H_2SO_4	no	225 °C	4 h	no
G12	0.5 M $Fe(SO_4)_{1.5}$ 0.05 M H_2SO_4	Fe_2O_3	225 °C	4 h	no
M60	0 5M $Fe(SO_4)_{1.5}$ 0.0 M H_2SO_4	no	220 °C	2 h	no

* M = molar fraction

† The stirring speed is 200 RPM for all the samples.

Guinier XRD. We analyze and report the CANMET results on the L samples to achieve a more global representation of the trends in (and correlations between) several key measured physical parameters.

The compositions of the hematites, reported as weight percent of Fe (wt% Fe) and of SO_4 (wt% SO_4), are given in Table 3.1.2. The presence of impurities seen by XRD is also noted in Table 3.1.2. These analyses were performed at CANMET. The samples typically contain 1-7 wt% of sulphate impurity whose exact chemical nature is not known.

On simple assumption of all Fe being in the form of Fe_2O_3, we first calculate the weight percent of Fe_2O_3 for each sample. The total wt% of (SO_4 + Fe_2O_3) is not 100% as might be expected. There is something else in the samples. Considering the nature of the powder samples, it is reasonable to suppose that the missing weight, wt% δ, is from adsorbed water. Both wt% Fe_2O_3 and wt% δ of water are also included in the Table 3.1.2. They will be corrected for the presence of other impurities in a later section (section 5.1.b).

Nominal pure bulk hematite (PBH) was investigated simultaneously to serve as a reference. Three commercial hematites were studied for this purpose. They were found to have essentially identical properties. These control samples were (i) At.Chem. (99.999 wt% Fe_2O_3), (ii) JMC

Table 3.1.2 Chemical composition of the samples†

Sample	wt% Fe	wt%SO_4	wt%Fe_2O_3*	wt%δ**	X-ray (Guinier)
G12	67.26	2.36	96.16	1.48	Fe_2O_3 + (minor $Fe(SO_4)(OH)$)
G1	66.20	1.64	94.65	3.71	Fe_2O_3
L9	65.64	4.05	93.85	2.10	Fe_2O_3
M60	62.65	3.70	89.57	6.73	Fe_2O_3
L10	67.40	2.45	96.36	1.19	Fe_2O_3
L7	64.98	4.38	92.90	2.72	Fe_2O_3+ (faint trace (~0.25%)$Fe(SO_4)(OH)$)
L1	64.71	6.29	92.52	1.19	Fe_2O_3+ (trace FeO.OH)
L3	62.09	6.98	88.77	4.25	Fe_2O_3+ (trace FeO.OH)

† Only wt%Fe and wt%SO_4 were measured: all other are derived quantities.

* wt%Fe_2O_3 is derived from the amount of iron in each sample.

** wt%δ is calculated by using (100% - wt%Fe_2O_3 - wt%SO_4).

(nominally pure), and (iii) BDH (General Purpose Reagent).

3.2 Scanning Electron Microscopy (SEM) of Ottawa Samples

To check the sample morphology, SEM was performed on the Ottawa samples at CANMET. The micrographs are shown in Fig.3.2.1 for loose powder mounts, and in Fig.3.2.2 for polished section mounts.

As seen in Fig.3.2.1 samples G1, L9 and M60 are aggregates consisting of many small particles stacked together. On the surface of the aggregates are varying degrees of roughness.

G12 consists of two distinct kinds of clumps: relatively large aggregates and very fine powdered hematite. This unique morphology is due to the presence of seed Fe_2O_3 in the synthesis of this sample (see Table 3.1.1). The large clumps are probably the new hematite produced on the surface of hematite seeds.

It is noted in Fig.3.2.2 that samples show various aggregate dimensions or mean sizes. The sizes range roughly from 3μm to 17μm in G1, 1μm to 5μm in L9 and 1μm to 30μm in M60. However, SEM results do not show any obvious correlations between sample shape/size/morphology and

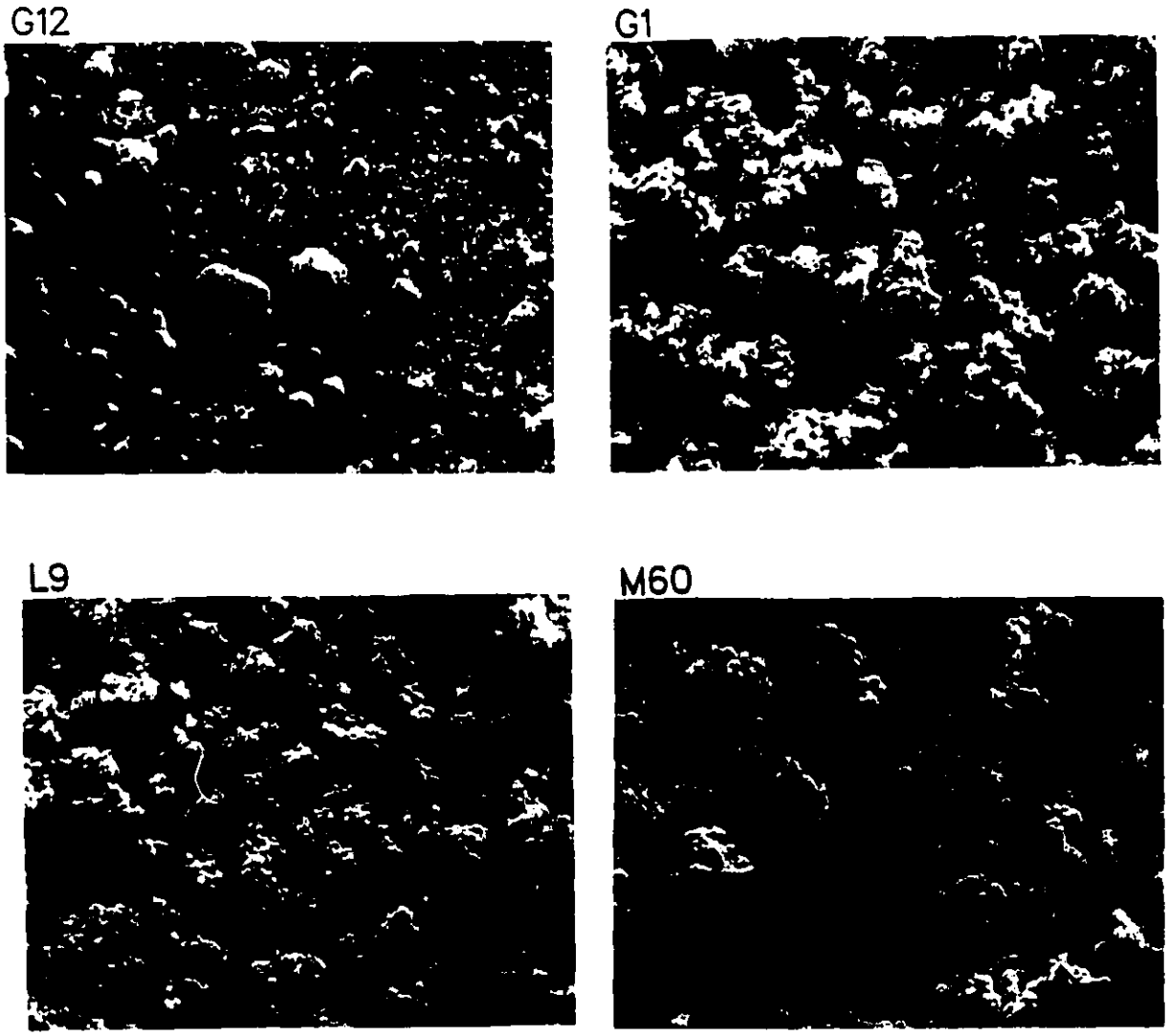

Fig.3.2.1 (a) SEM pictures of Ottawa samples in loose powder mounts at low magnification.

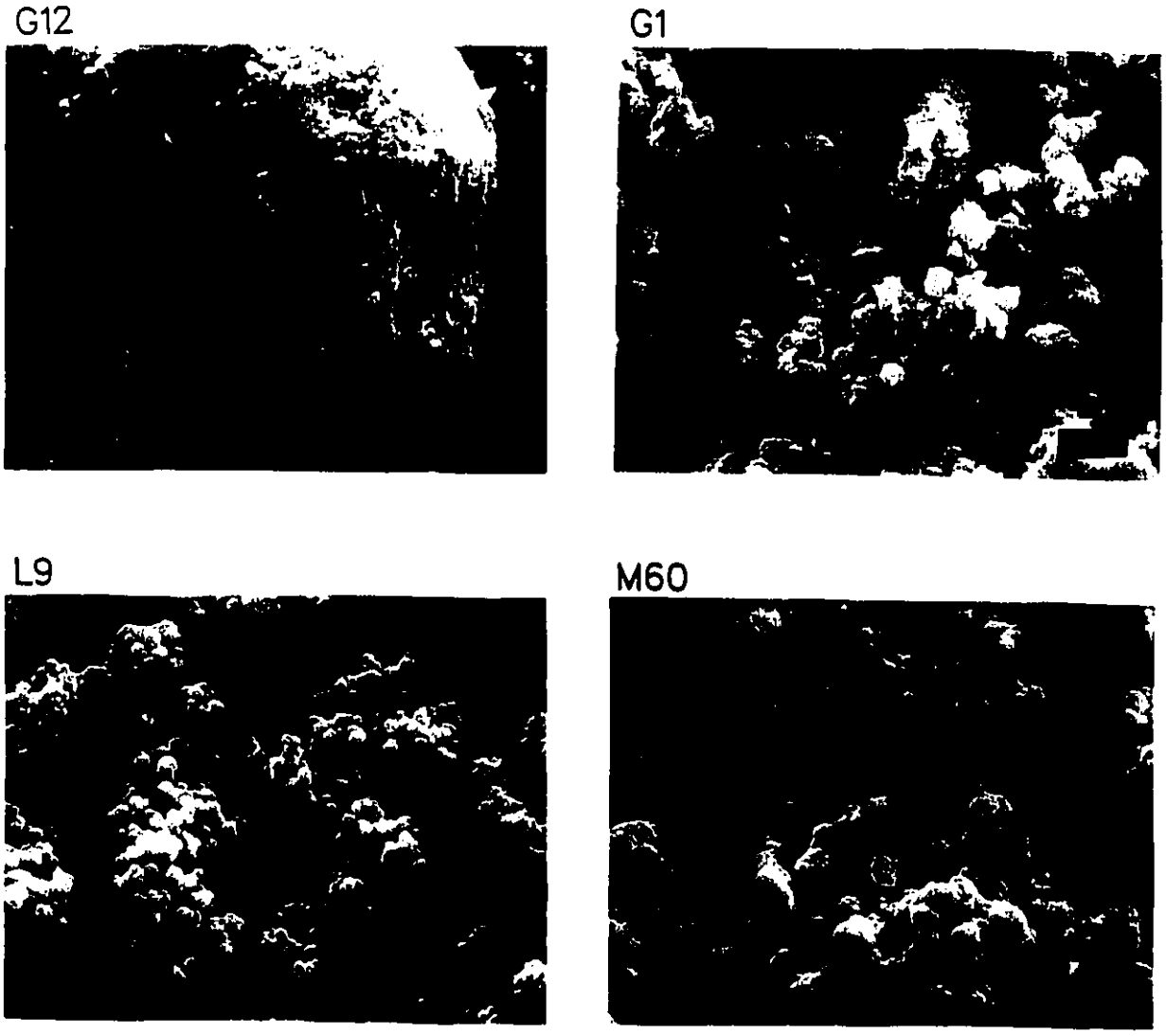

Fig.3.2.1 (b) SEM pictures of Ottawa samples in loose powder mounts at high magnification.

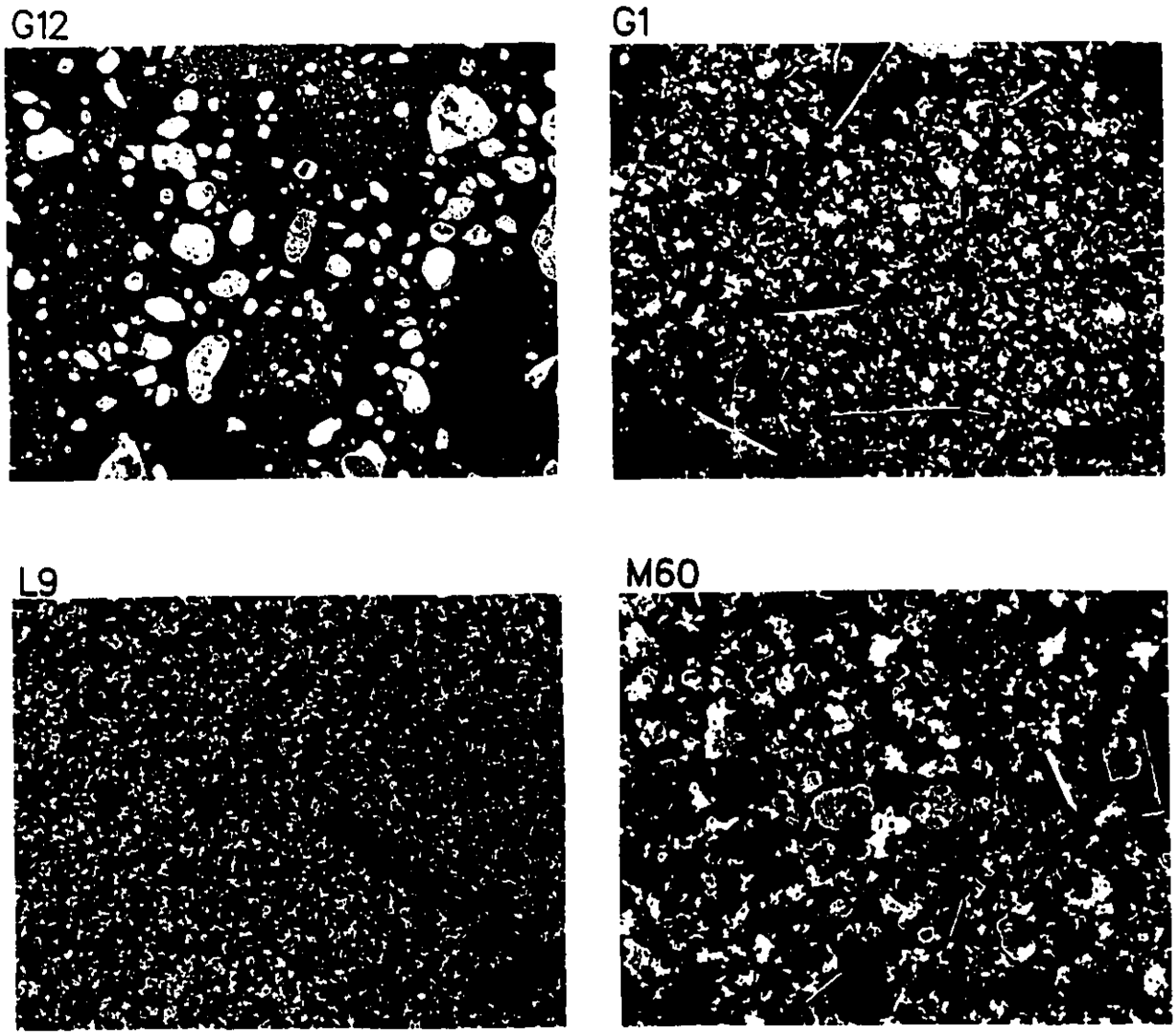

Fig.3.2.2 (a) SEM pictures of Ottawa samples for polished section mounts at low magnification.

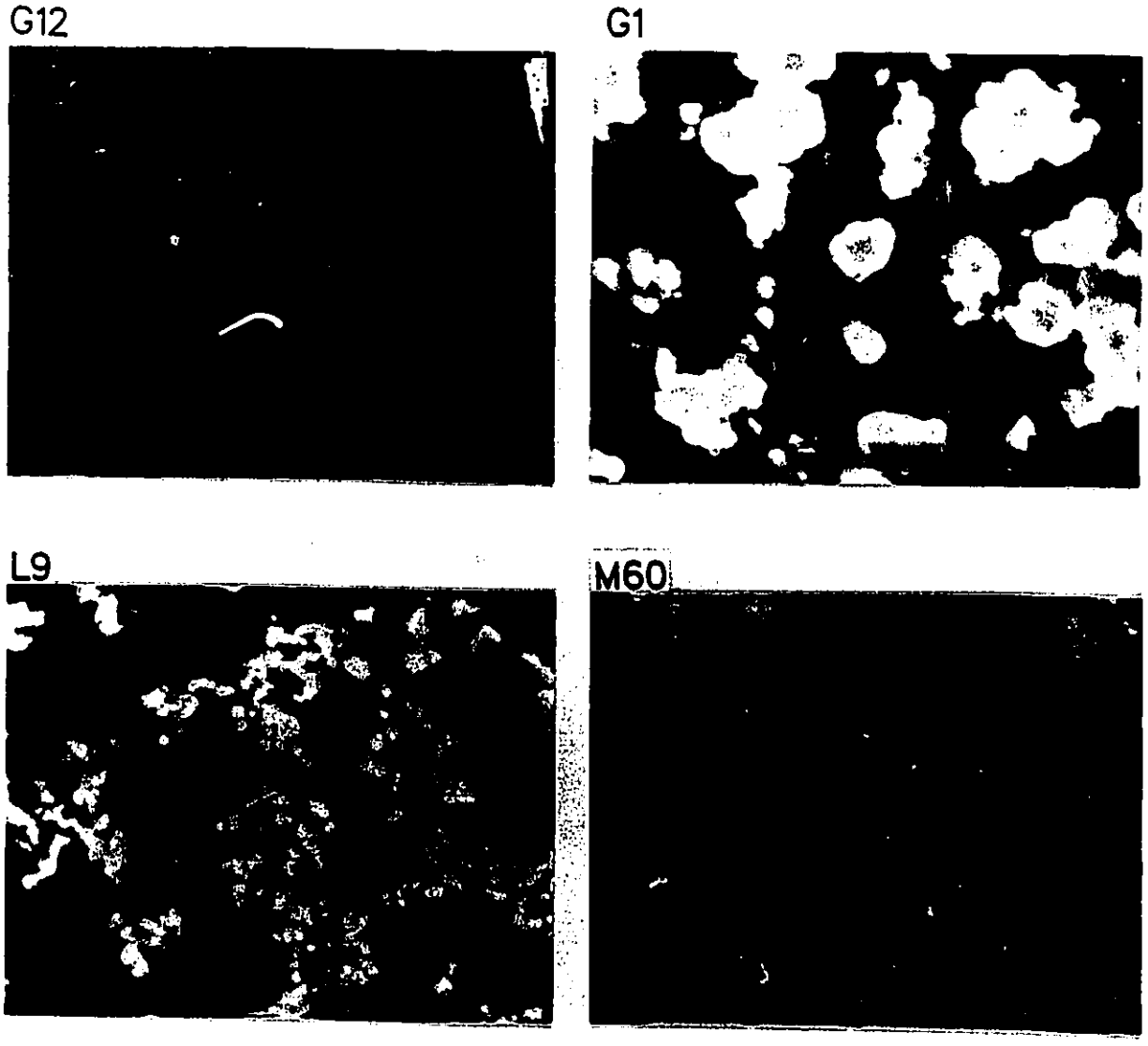

Fig.3.2.2 (b) SEM pictures of Ottawa samples for polished section mounts at high magnification.

overall sample impurity content.

Differences in brightness seen in Fig.3.2.2 suggest that there are some differences of local density, compactness and crystallinity in the different sampples.

3.3 X-Ray Diffraction (XRD) Results

Powder XRD experiments were carried out by Dr. H. Kodama at Agriculture Canada with an automated Scintag diffractometer using Co $K\alpha_1$ radiation from a post-sample monochromator. Only the Ottawa samples were studied here.

XRD results shown in Fig.3.3.1 indicate that, structurally, all samples are crystalline hematite (α-Fe_2O_3), since the X-ray patterns coincided closely with a standard α-Fe_2O_3 reference pattern. The compilation of X-ray powder patterns for minerals by the Joint Committee on Powder Diffraction Standards (JCPDS) was used to identify crystalline phases.

In Fig.3.3.1, it is observed that the diffraction lines are clearly getting weaker and broader in the sequence PBH, G12, L9, G1 and M60, for identically mounted samples. We choose three intense lines and three weak lines to specify this point quantitatively. Table 3.3.1 gives these

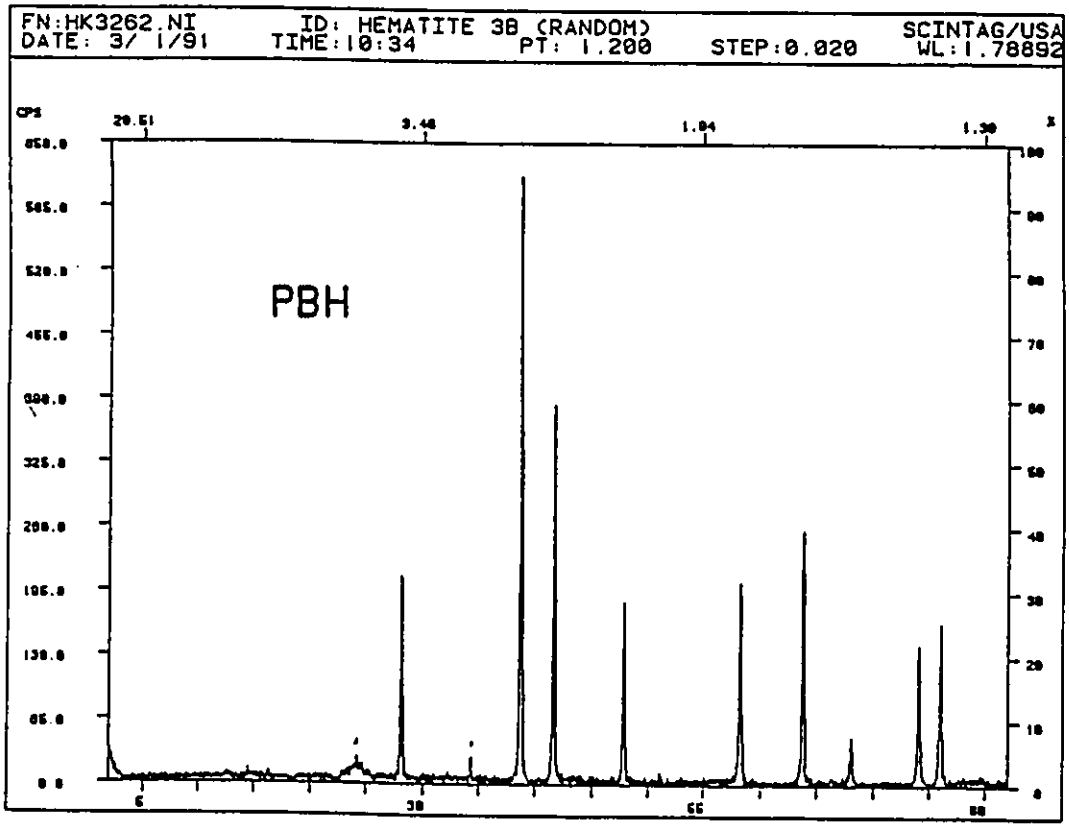

Fig.3.3.1 XRD patterns of the Ottawa samples.
(a) XRD pattern of PBH.

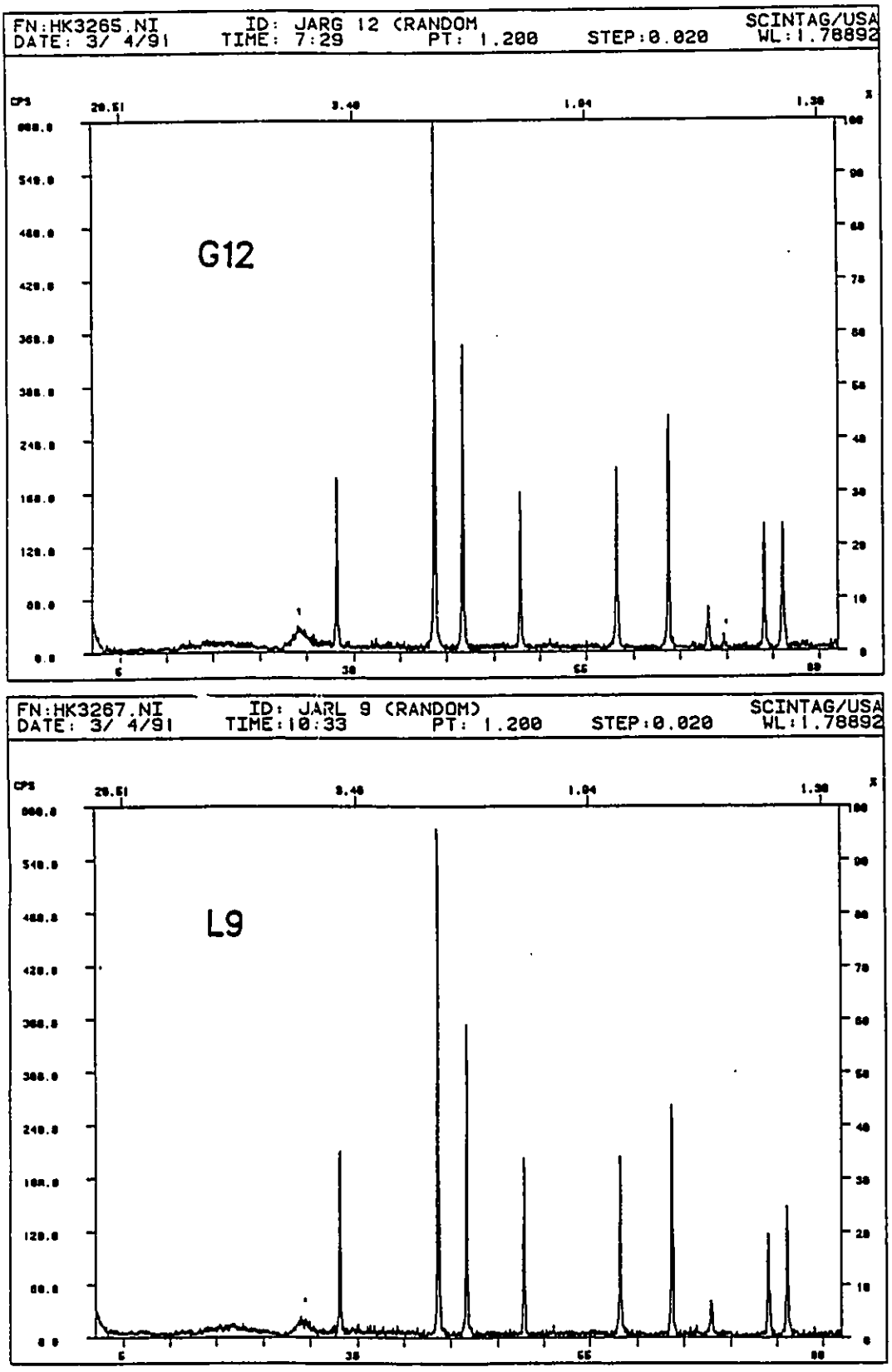

Fig.3.3.1 (b) XRD patterns of G12 and L9.

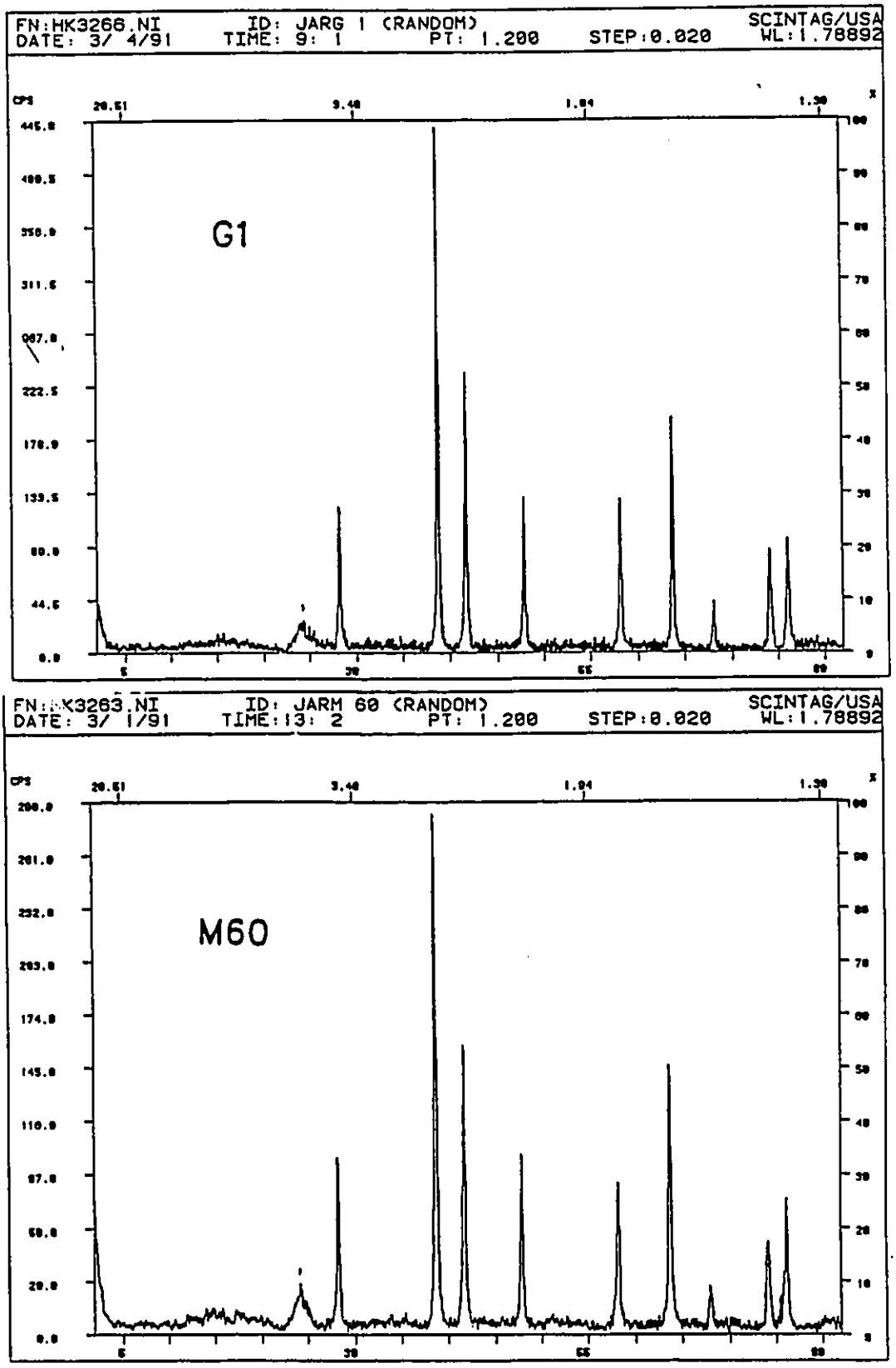

Fig.3.3.1 (c) XRD patterns of G1 and M60.

Table 3.3.1 XRD results for certain line widths and heights

Sample	θ^*_1	θ_2	θ_3	θ_4	θ_5	θ_6
PBH	.201	.212	.237	.280	.226	.226
G12	.201	.212	.237	.339	.226	.226
L9	.201	.212	.237	.341	.262	.262
G1	.255	.266	.280	.341	.399	.399
M60	.309	.323	.352	.517	.474	.424

Sample	H1†	H2	H3	H4	H5	H6.
PBH	620	387	260	52	145	167
G12	604	350	267	51	144	144
GL9	577	357	263	42	119	149
G1	440	234	197	44	86	96
M60	283	158	146	27	52	74

* θ is the angular width of the line in degrees, error is 0.007°.

† H is the height expressed in counts per second.

Indices 1, 2, 3 represent the first, second and third most intense lines, respectively,at 38.5°, 41.5° and 63.5° of 2θ. Indices 4, 5, 6 represent the weakest line, the second weakest and third weakest lines, respectively, at 68°, 74° and 76° of 2θ.

line full widths at half maximum and line heights.

It is known that XRD patterns depend on the sample crystallinity. A high degree of crystallinity in bulk samples gives intense and sharp lines. Whereas broader and weaker lines arise from either (i) crystal inhomogeneities and imperfections such as substitutional disorder, impurities, and vacancies, or (ii) from small crystal sizes on a scale of several hundred Angstroms or less.

Both effects may occur simultaneously in our case. If they are comparable in magnitude, separation of these effects is difficult. Nevertheless, SEM reveals that the aggregate dimensions in the samples do not vary in the XRD sequence (PBH, G12, L9, G1, M60). Moreover, Sherrer's formula gives that the broadening of the diffraction lines from the crystal size effect increases with increasing Bragg angle θ (Guinier 1963). But in Table 3.3.1 the line width does not change in this way, particularly for the three weak lines. All of these suggest that crystal imperfections are more important and dominant. Therefore, we will describe our samples in terms of an effective crystal quality.

XRD reveals that G12, except for having a distinct impurity phase that corresponds to a small amount of $Fe(SO_4)(OH)$ (as seen in both the Mössbauer spectrum and the XRD pattern itself), is the closest to PBH in terms of crystal quality. Chemically, it also has the least impurity

contents of sulphate and water. L9 is apparently better crystallized than G1, but its impurity content is higher than that of G1. M60 is clearly the last: both in the sequence of effective crystal quality and in impurity content.

Additionally at small angles of diffraction ($2\theta \simeq 24^{\circ}$) there is a small bump observed in all samples that is not due to a contribution from the sample holder. Given its width, it should correspond to a quasi-amorphous material. By checking the position and intensity with JCPDS, it is probably a particular iron sulphate compound: $Fe_2(SO_4)_3.11H_2O$, called quenstetite. Its relative intensity decreases from M60 to PBH.

4. EXPERIMENTAL METHODS FOR MÖSSBAUER SPECTROSCOPY

4.1 Equipment

Transmission Mössbauer spectra were taken at room temperature (RT) and liquid nitrogen temperature (LT) with a 10 mCi source of Co-57 in a rhodium matrix. The spectrometer was operated in a constant acceleration mode. Data was accumulated in 1024 channels. The Doppler velocity scale was from -10 mm/s to 10 mm/s.

An Fe-57 enriched metallic iron foil was used for calibration of the spectrometer before and after each spectrum. Line positions (LP) are given with respect to the center of the calibration spectrum (i.e. relative to α-Fe at room temperature). The spectra were folded in order to obtain a flat background. Non-linear fitting was performed with the Minuit software package developed at CERN (James 1975).

For LT experiments, a cold-finger cryostat was operated with two temperature sensors serving for temperature measurement. The temperature was measured by a diode and a thermocouple, both attached to the sample block. The temperature variations over the course of an experiment (typically 24 hours) were less than ±1 K. The temperature gradient cross the absorber was less than 1 K across a 3/4

inch diameter.

4.2 Absorber Preparition

Two kinds of absorbers were used in the experiments. They were prepared as follows.

(I) For the absorbers only run without the cryostat at RT: 100 ± 1 mg of sample was spread evenly and sandwiched between two clear plastic sheets held in aluminum holders with 3/4 inch diameter windows.

(II) Some absorbers were prepared for LT and RT measurements in the cryostat. A pan of 3/4 inch diameter was made of (usually ultra pure) metallic aluminum foil in which a little grease was melted on a hot plate. Then 125 ± 1 mg of sample was stirred evenly with the grease. Then another aluminum foil was put on the top. A brass ring with 3/4 inch inside diameter was used to hold the pan. These absorbers were mounted inside the cryostat for both RT and LT experiments.

5. RESULTS AND DISCUSSION

5.1 Room Temperature Mössbauer Study

a. Spectral features of Ottawa samples and L samples

The first series of measurements consisted in collecting Mössbauer spectra at RT. The spectra for the Ottawa samples were taken in our laboratory while the spectra of the L samples were taken at CANMET. All the spectra are shown in Fig.5.1.1.

Each of the RT spectra is basically a magnetic sextet pattern, which is similar to that of PBH. The spectra are not collapsed as in the case of superparamagnetism. Hence, the effective particle size for all samples is greater than 200 Angstroms (Kundig et al., 1966).

Following the usual convention for sextets, we number the lines from 1 to 6 starting at the lowest Doppler velocity (see Fig.2.3.1). On comparing the spectra in detail, it is observed that the absorption lines are broadened and asymmetric. This is most noticeable in lines 1 and 6. The degree of broadening increases progressively on going from PBH to M60 in the Ottawa samples or from L10 to L1 in the L samples in the general sequence of increasing impurity content.

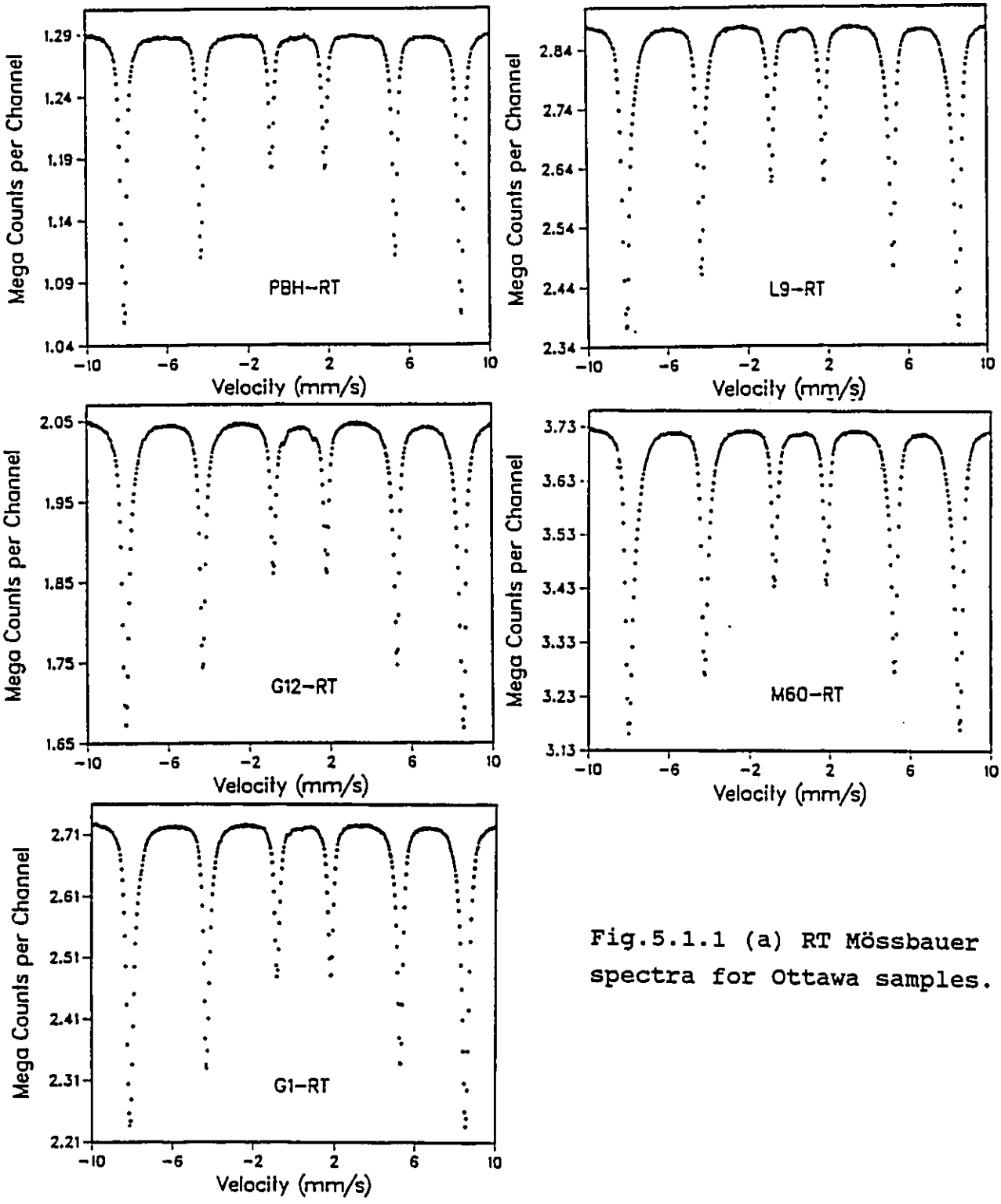

Fig.5.1.1 (a) RT Mössbauer spectra for Ottawa samples.

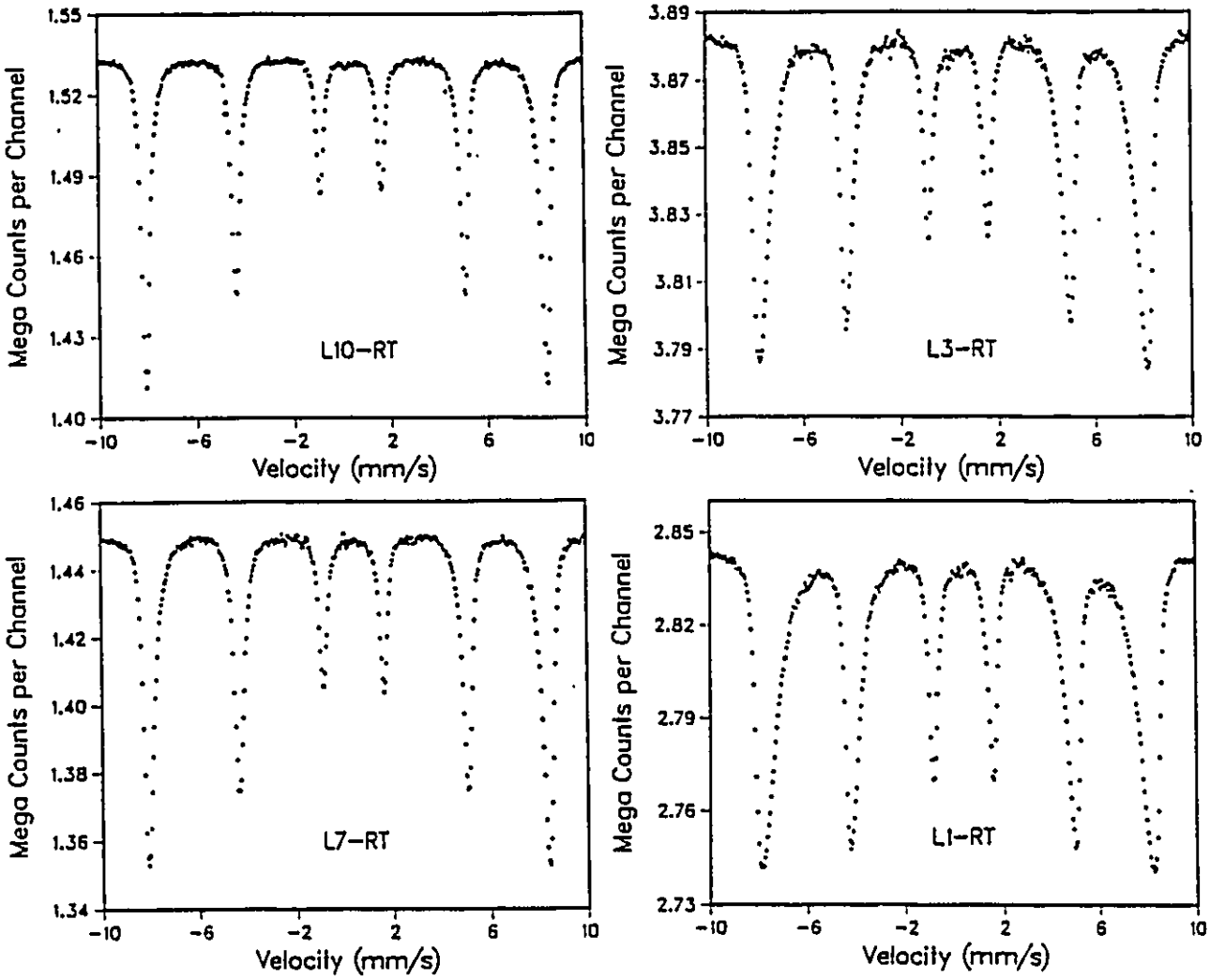

Fig.5.1.1 (b) RT Mössbauer spectra for L samples.

To emphasize sample to sample differences, the line-1 of the spectra are plotted together in Fig.5.1.2. Fig.5.1.2a shows the line-1 for the Ottawa samples and PBH, whereas Fig.5.1.2b shows the line-1 for the L samples compared to line-1 for PBH. It is seen clearly that the impurity content of a sample is significantly correlated to its Mössbauer spectrum.

Comparing the line width and the line position with the given chemical analysis (Table 3.1.2) for each sample, we found that it is the total sample impurity (or degree of hematite purity) rather than just wt% SO_4 or wt% δ that affects these spectra systematically.

By measuring the line-1 width and the line-1 position for different samples, some quantitative phenomenological relationships are obtained. Figs 5.1.3a and b show how the line-1 full width at half maximum (FWHM) and position (i.e. the minimum of line-1) vary with the overall sample purity (wt% Fe_2O_3). The dotted lines are the best straight line fits. They give the following equations:

$$\text{FWHM} = (0.29\ \text{mm/s}) + (0.038\ \text{mm/s per wt\%}) \cdot \text{wt\%}(SO_4 + \delta) \qquad (5.1.1)$$

$$\text{LP} = (-0.82\ \text{mm/s}) + (0.024\ \text{mm/s per wt\%}) \cdot \text{wt\%}(SO_4 + \delta) \qquad (5.1.2)$$

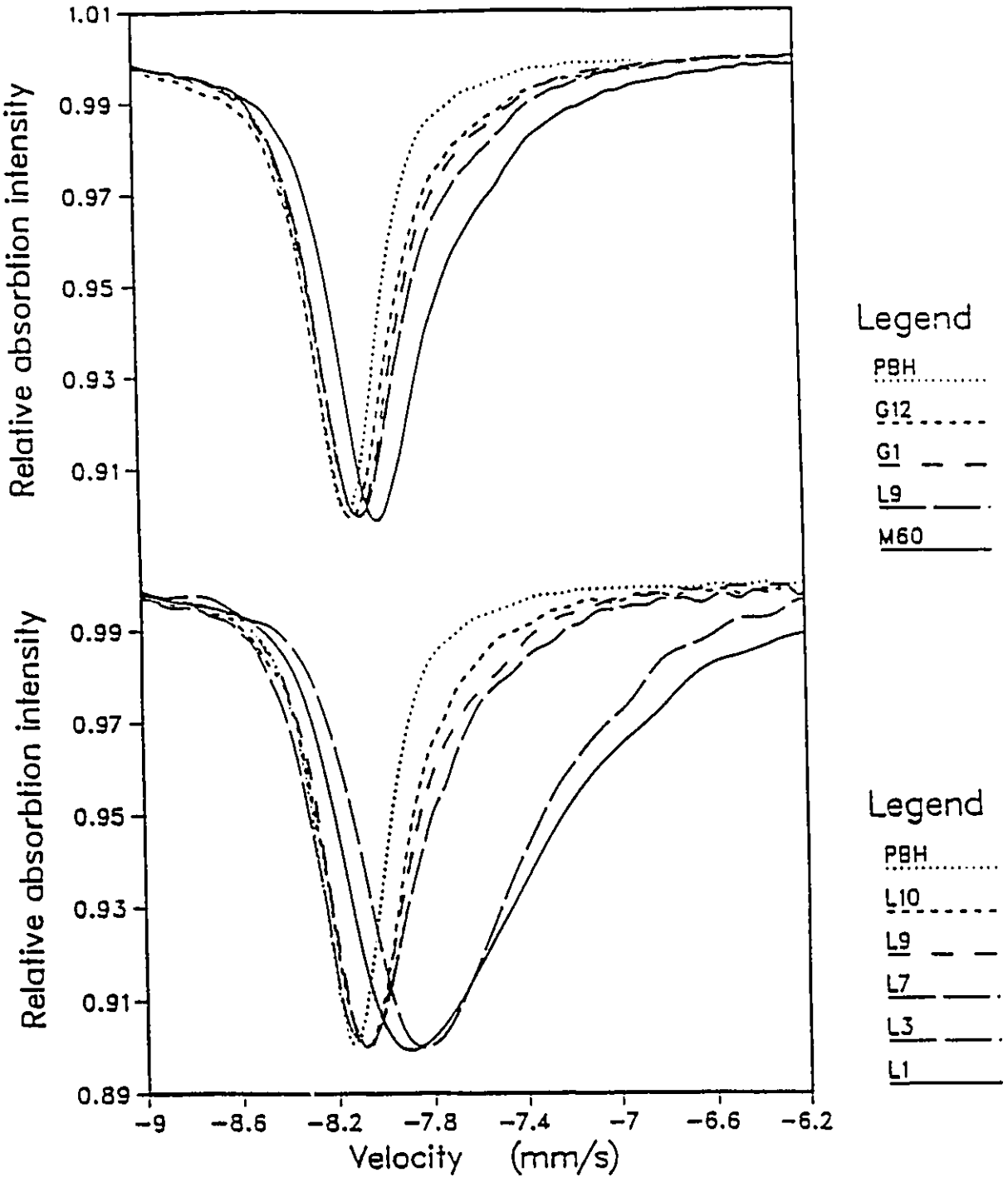

Fig.5.1.2 RT spectral line-1 for Ottawa samples (top) and for L samples (bottom) compared to PBH.

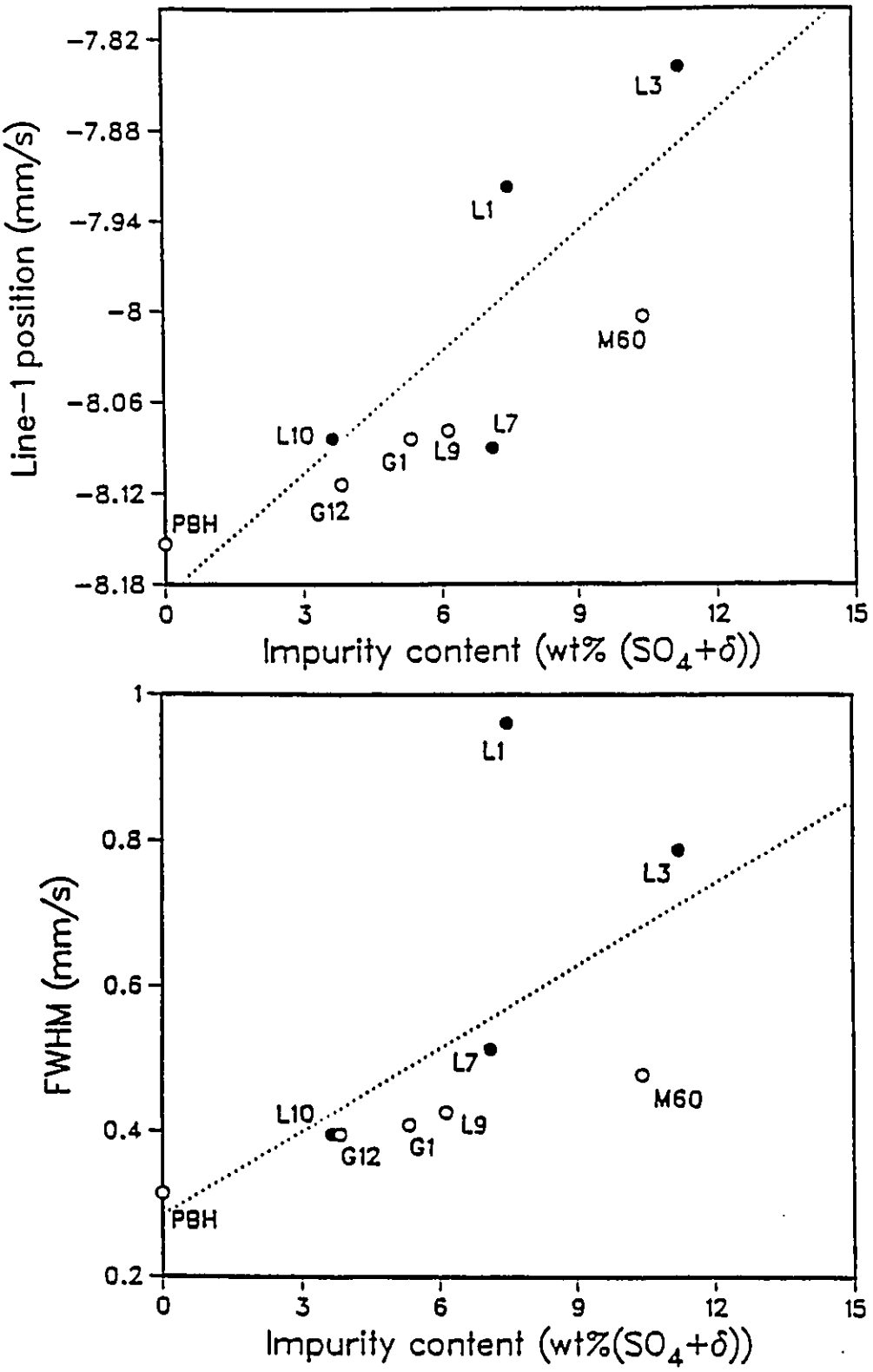

Fig.5.1.3 (a) RT line-1 positions versus sample impurity content based on the wt% Fe from the chemical analysis. (b) RT line-1 width versus sample impurity content.

These equations will be improved after further investigation on the impurities in the next section. But the conclusion that the spectra are affected by the total content of impurities rather than just wt% SO_4 or wt% δ is not changed by the composition recalculations based on supposed/suspected/observed additional impurities, although the best quantitative relations are changed significantly (section 5.1.b).

b. Searching for impurities and correcting the compositions

First we focus on the Ottawa samples. Based on XRD analysis, there is a minor amount of $Fe(SO_4)(OH)$ in G12. Also, a very small amount of quenstetite ($Fe_2(SO_4)_3.11H_2O$) is probably seen in the Ottawa samples by our XRD (section 3.3). Chemically, some other impurities are possible in the samples. For example, ferrous sulphate ($FeSO_4$) and crystalline and amorphous $Fe_4(SO_4)(OH)_{10}$. The spectra of these possible or likely impurities were recorded for identifying them in the samples. These RT spectra are shown in Fig.5.1.4.

In the spectrum of G12, a doublet is indeed observe.. in addition to the main hyperfine six-line pattern. Comparison

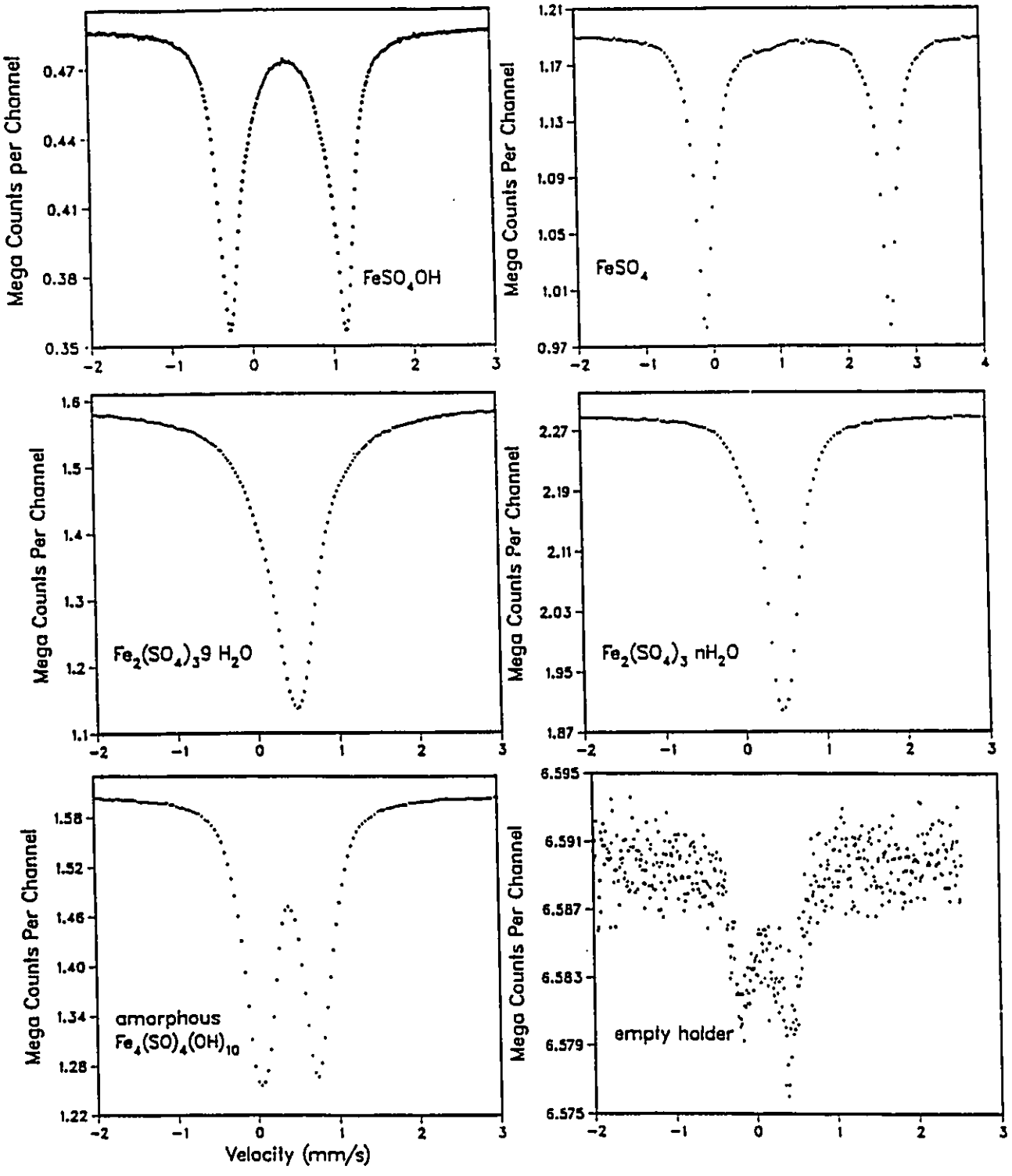

Fig.5.1.4 RT Mössbauer spectra of some possible or known impurities.

with the spectrum of $Fe(SO_4)(OH)$ in Fig.5.1.4 proves that this doublet results from $Fe(SO_4)(OH)$, and this agrees with the XRD from CANMET.

In the spectra of G1, L9 and M60, there is no such doublet as that showing in G12. No amount of $Fe(SO_4)(OH)$ (detectable by Mössbauer or any other method used) was therefore seen in any of the other Ottawa samples. But in the central area of the spectra, from -0.2 mm/s to 0.6 mm/s, there are very weak signals. Since these are seen in all the spectra, they are suspected to arise from an impurity of quenstetite $Fe_2(SO_4).11H_2O$ whose presence is suggested by our XRD results (section 2.3).

As shown in Fig.5.1.4 the spectrum of nominal $Fe_2(SO_4)_3.nH_2O$ is a singlet at about 0.46 mm/s. The spectra of $Fe_2(SO_4)_3.9H_2O$ and $Fe_2(SO_4)_3.7.25\ H_2O$ are also singlets, but the widths and positions are slightly different. It seems that increasing the water content causes the lines to be broader and to shift to lower Doppler velocities. This suggests that the singlet of quenstetite would be right in the impurity signal range (-0.2 to 0.6 mm/s).

We also run the empty holder in the same set-up. It is seen, unfortunately, that there is a doublet showing up as shown in Fig.5.1.4. Its lines are at about -0.16 mm/s and 0.4 mm/s, right in the impurity signal area. This doublet most probably arises from iron impurities in the beryllium

window of our gas proportional counter. Its high energy line is very close to the position of the quenstetite singlet. They both may cause the very weak absorption observed here.

In this case, we can only say that impurity quenstetite may or may not be present. If the weak signals result from both the empty holder and impurity quenstetite, then from the relative area ratios of an assumed quenstetite singlet to the hematite sextet, the calculated iron amount in this impurity (assuming equal f-factors) is about 0.2 wt%. This is very close to the detection limit. If all signals are due to the empty holder, then the quenstetite impurity is not detected because of its small amount and/or lower f-factor.

$Fe(SO_4)$ and amorphous and crystalline $Fe_4(SO_4)(OH)_{10}$ do not show any traces at all, that is consistent with XRD results and chemical analyses.

With a given content of wt% SO_4 from a chemical analysis, the iron amount in a sulphate impurity can be calculated from the impurity's stoichiometry. In this way, the iron amount in $Fe(SO_4)(OH)$ was calculated for G12. A corrected hematite content can thereby be obtained for this sample.

Since there is evidence of quenstetite from both Mössbauer and XRD in samples G1, L9 and M60, then the iron

amounts in the supposed quenstetite impurity were calculated from the given wt% SO_4 in each sample, . This accounts for the sulphur contents of these samples in the most reasonable way we have found and it leads to slightly corrected Fe_2O_3 contents. And in G12 (see above) $Fe(SO_4)(OH)$ was our prime candidate as the main sulphur containing material.

For the L samples, impurity contents and composition corrections were obtained in three ways. (i) The impurity $Fe(SO_4)(OH)$ was seen in L7 by XRD. The corresponding amount of iron in $Fe(SO_4)(OH)$ was calculated from the given wt% SO_4 as in G12. (ii) For L1, L3 and L10, the sulphate impurity was assumed to be quenstetite and the relevant corrections were done as for G1, L9, and M60 above. (iii) For L1 and L3, an additional impurity of FeO.OH was detected by XRD. This compound gives a six line pattern in its RT Mössbauer spectrum (Morup 1983). This impurity six line pattern visibly distorted our spectra. Its amount is more significant than that of the sulphate impurity. To get an iron amount in this impurity, the spectra were fitted with a hematite sextet and an FeO.OH pattern with its parameters frozen at the known values. The resulting iron amounts in FeO.OH are approximately 8 ± 2 and 4 ± 2 wt% in L1 and L3 respectively.

In these ways, all the supposed (and/or measured) impurities were taken into account to obtain a correct

Table 5.1.1 Corrected chemical compositions

sample	wt% Fe given	wt% SO_4 given	wt% Fe_2O_3 calculated (a)	wt% Fe (b)	wt% Fe in Fe_2O_3 (c)	wt% Fe_2O_3 corrected
G12	67.26	2.36	96.16	1.38±.17	65.88±.17	94.19±.34
G1	66.20	1.64	94.65	0.64±.14	65.56±.13	93.73±.29
L9	65.64	4.05	93.85	1.57±.40	64.07±.40	91.60±.57
M60	62.65	3.70	89.57	1.44±.28	61.21±.31	87.51±.44
L1	64.71	6.29	92.52	2.44±1.04 8.50±2.00	53.82±3.04	76.95±1.56
L3	62.09	6.98	88.77	2.71±1.10 4.30±2.00	55.11±3.01	78.79±1.61
L7	64.98	4.38	92.90	1.70±.54	63.28±.50	90.47±0.78
L10	67.40	2.45	96.36	0.95±.29	66.45±.30	95.00±0.41

(a) Assumes that all the iron is in the hematite. It is obtained directly from the measured (given) wt%Fe.

(b) This part is the iron amount in one or more impurities. In most cases, it is calculated from the stoichiometry of the relevent impurity, given the known sulphur amount. In L1 and L3, iron amounts are in two impurities: FeO.OH and quenstetite. Qenstetite $Fe_2(SO_4)_3.11\ H_2O$ is used to calculate the iron amount in the sulphate impurity for all the samples except G12 and L7 where $Fe(SO_4).OH$ is known to be the main impurity.

(c) This is the total amount of iron in the hematite after correction.

hematite amount for each sample. The corrected compositions are given in Table 5.1.1 and compared to the raw values based solely on wt% Fe from the chemical analyses.

In fact, both sulphate impurities $Fe_2(SO_4)_3.11H_2O$ and $Fe(SO_4)(OH)$ may coexist in all the samples. The various ways of accounting for this coexistence or for small amounts of other similar sulphur impurities do not change the resulting corrected Fe_2O_3 amounts by more than the errors quoted in Table 5.1.1.

Our impurity corrections do not change our main conclusions and only improve the observed correlations between measured quantities such as line positions and line widths, quadrupole splittings, HFD characteristics, etc.— at both RT and low temperature (section 5.2).

For example, Fig.5.1.5 is a new plot (that can be compared to Fig.5.1.1) of the line-1 position and FWHM as functions of the corrected purities. Two best-straight-line fits give new equations that can be compared to Eqs.5.1.1-2:

$$\text{FWHM} = (0.25\ \text{mm/s}) + (0.027\ \text{mm/s per wt\%})\cdot\ \text{wt\%}(SO_4 + \delta) \qquad (5.1.3)$$

$$\text{LP} = (-0.82\ \text{mm/s}) + (0.013\ \text{mm/s per wt\%})\cdot\ \text{wt\%}(SO_4 + \delta) \qquad (5.1.4)$$

These expressions and Fig.5.1.5 suggest that the impurities (whatever their precise nature) "cause" the observed

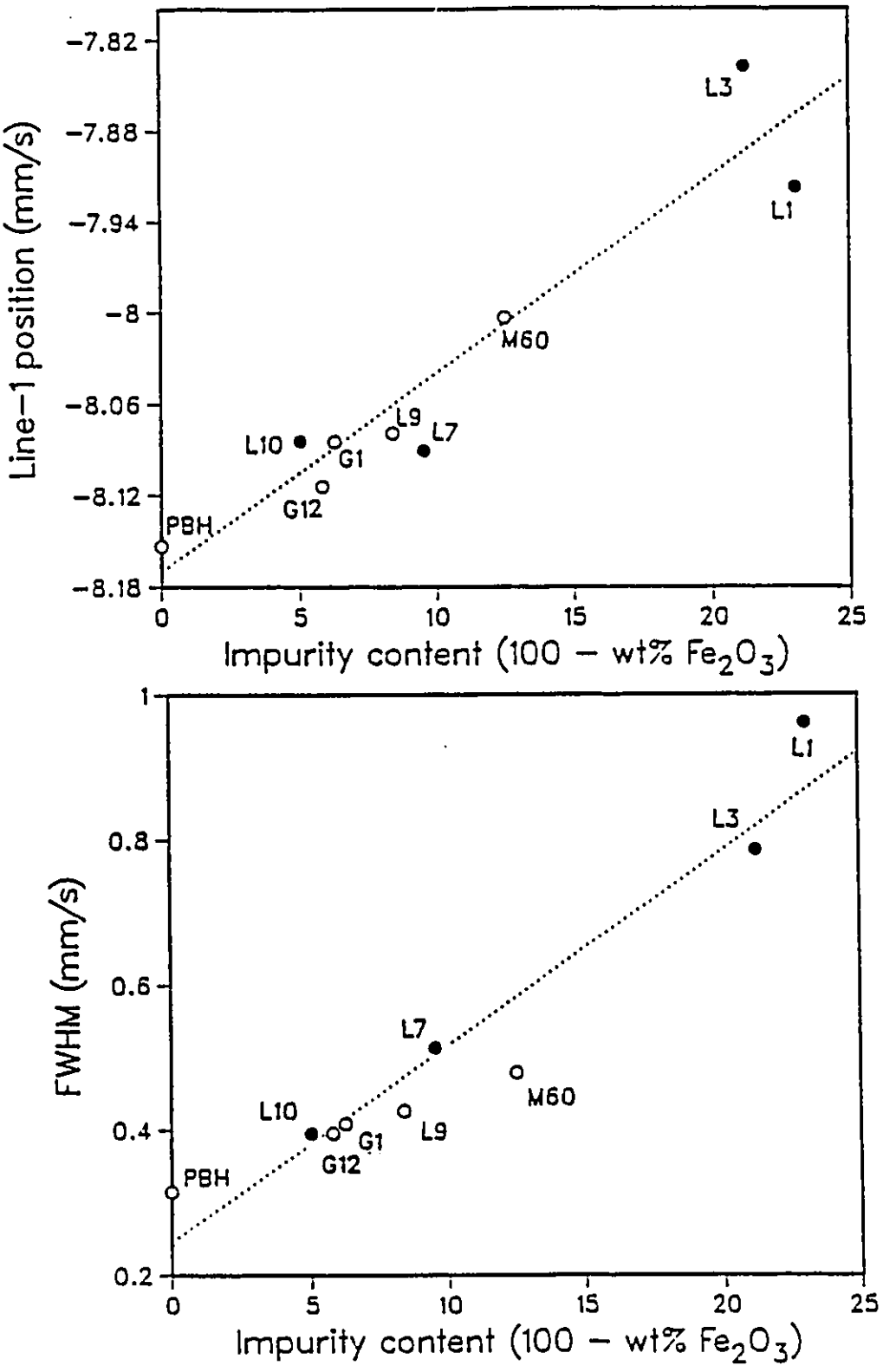

Fig.5.1.5 (a) RT line-1 position and (b) line-1 width versus the impurity content based on the corrected sample purity; as given in Table 5.1.1.

broadening of the hematite sextet lines, however, such an interpretation is not correct. Although there are impurities in all of these hematites and although the spectra show correlations to the impurity contents, the impurities can not cause the line broadening directly because virtually all of the iron in the "hematite" takes part in this line broadening.

We find that our RT spectra are broadened similarly to the spectra broadened by surface effects reported by Jiang et al. (1987). The surface is a kind of defect where iron ions near the surface lose their nearest neighbors or next near neighbors and are in octahedral environments significantly different from those in the bulk. This implies that our samples have a very high effective surface density (in cm^2 of effective surface per gram of Fe_2O_3) or an equivalent density of vacancies. Both the effective defect density (or porosity or compactness) of the hematite and the net weight fraction of impurities depend on the precise synthesis route and conditions, and are therefore related.

We next describe detailed lineshape analysis of the RT spectra in an effort to learn as much as possible about our "surface" ions (i.e. that are either near a surface or near a defect).

c. Fitting results for the Ottawa samples

In the RT spectra only PBH has a well defined hyperfine pattern corresponding to single site hematite. The other spectra are broadened to various degrees, indicating HFD's arising from various different local environments of the Fe probe. This is expected to be related to specific surface density, sample purity, and crystallinity. We apply a new HFD method (Rancourt and Ping, 1991) to analyze the spectra of the Ottawa samples.

The moderate broadening of the spectra for the Ottawa samples suggests that the different local environments for iron are not much different from the single iron site environment in PBH. Basically all the iron consists of magnetically ordered Fe^{3+} ions in hematite sites that are only somewhat distorted compared to PBH. Therefore we choose a "one site" model with two Gaussian components (section 2.5) to fit the spectra.

Two groups of the RT spectra need fitting. One is the group in which absorbers were mounted outside the cryostat. The other is a group run in the cryostat at RT for comparison with the LT spectra.

Since we are most interested in the systematic sample to sample changes, certain physical and reasonable constraints have been tried to avoid the trade off problem of dependent

fitting parameters. (i).The couplings between the CS and z, and between ε and z are taken to be zero (i.e., $\delta_1 = \varepsilon_1 = 0$ in Eqs.2.5.2 and 2.5.3). (ii).The intensity ratios R1 (line-1/line-3) and R2 (line-2/line-3) are taken to have certain fixed physical values as described below.

The first constraint forces the center shifts and quadrupole splittings not to have coupling to the distributed hyperfine field. As a result, there are no associated distributions of either center shift or quadrupole splitting.

The second constraint arises from the following considerations. Two different amounts (100 mg and 125 mg) of the samples were used for the two groups of absorbers. It is known that only when an absorber is ideally thin are thickness effects negligible. In this case the predicted intensity ratios for random powders are R1 = 3 and R2 = 2. But the absorbers are not ideally thin such that thickness effects will lower the ratios R1 and R2. Therefore we reached useful area ratio constraints by two steps. First we fit the spectra with R1 and R2 in the imposed ranges of 2.6 to 3 and 1.6 to 2, respectively, and then froze R1 and R2 at the values of their averages over all the spectra, and fit the spectra again.

Our final fitting results are obtained with the one-site two-component HFD model having the above

constraints. Fig.5.1.6 shows the fitted spectra. The corresponding HFD's are shown in Fig.5.1.7, along with the HFD obtained from subjecting our PBH to the same analysis (with only one site and one component however). The corresponding fitting parameters are listed in Table 5.1.2. They show that even though there are some differences between the two groups of samples for the two different experimental conditions, some general trends are obtained. These are described as follows.

(A). In our one-site fits, the two HFD components are very different (Fig.5.1.7).

The first one is centered on a higher field value, has a narrower distribution width, and presumably corresponds to local environments most similar to those of the single site in PBH. We call it the PBH-like HFD component. As seen in Fig 5.1.7, the majority of the iron in the Ottawa samples is in PBH-like local environments since the PBH-like component makes up the largest fraction of the total HFD.

The second component has a lower average hyperfine field and a larger distribution width. It is probably correlated to the various defects and will be referred to as the defect HFD component. It appears as broad low field bumps in the distributions shown in Fig.5.1.7.

(B). The spectral area ratio of the PBH-like HFD component (defect HFD component) decreases (increases) on

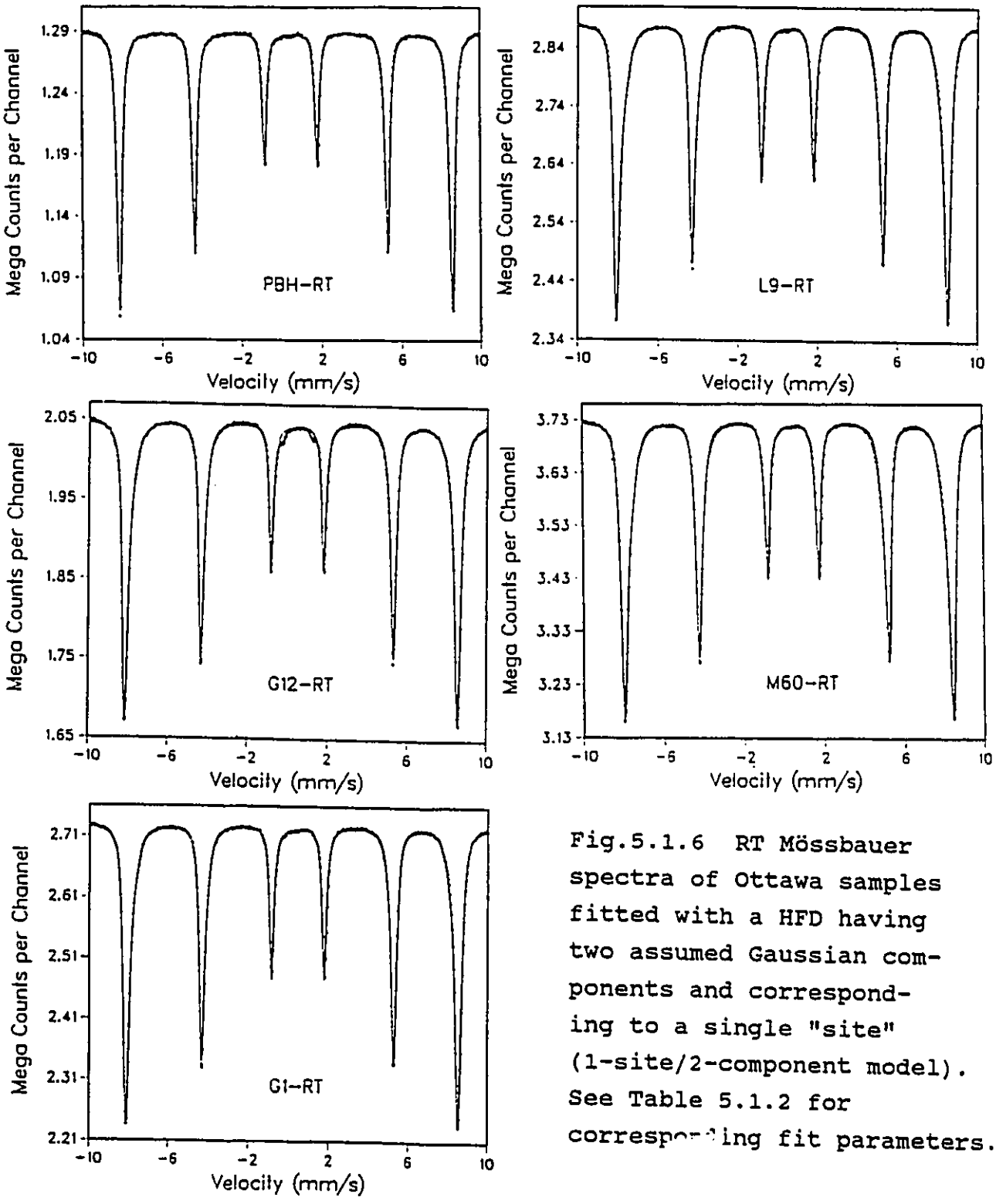

Fig.5.1.6 RT Mössbauer spectra of Ottawa samples fitted with a HFD having two assumed Gaussian components and corresponding to a single "site" (1-site/2-component model). See Table 5.1.2 for corresponding fit parameters.

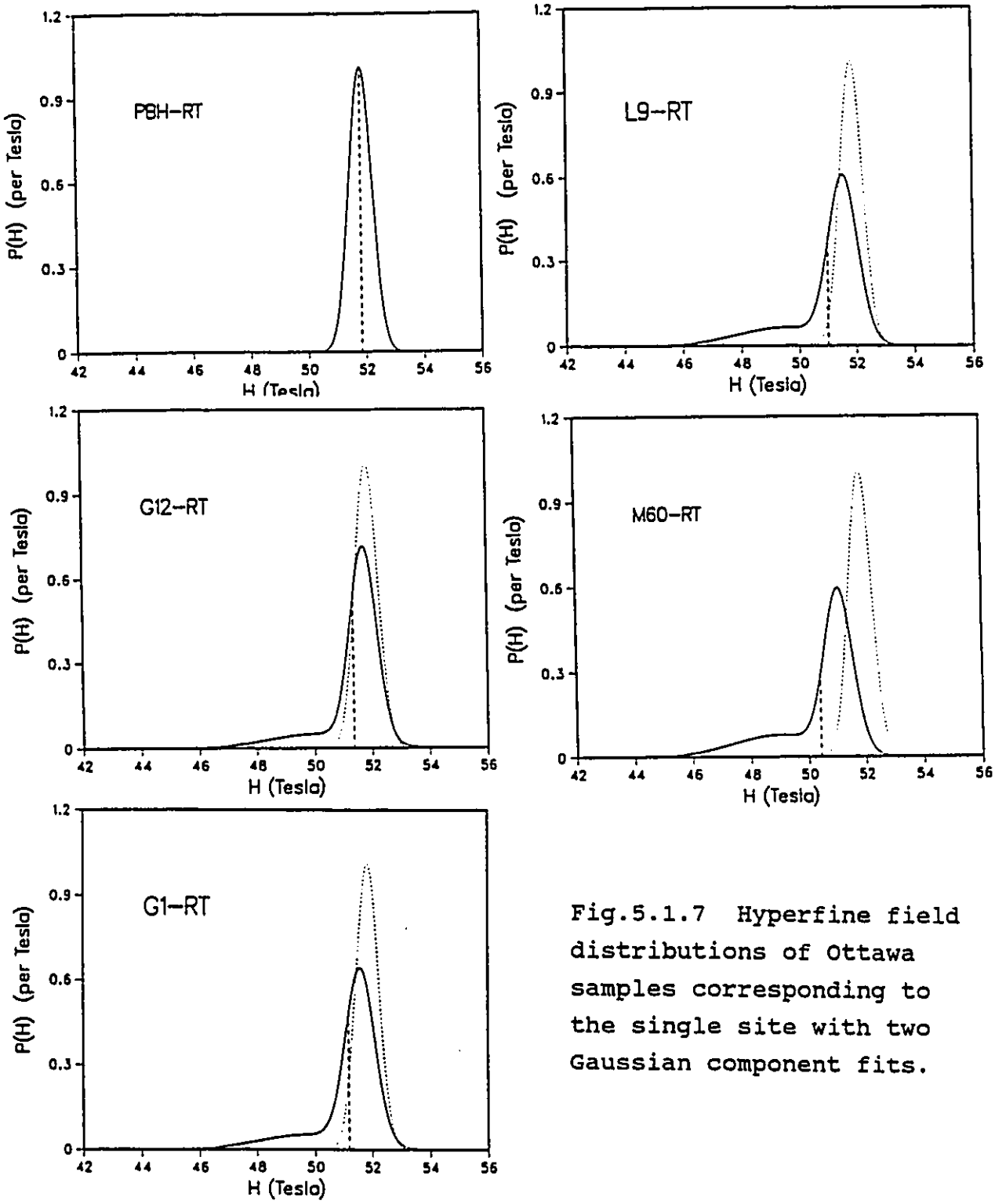

Fig.5.1.7 Hyperfine field distributions of Ottawa samples corresponding to the single site with two Gaussian component fits.

Table 5.1.2 RT fit parameters for 1-site/2-component HFD fits of the Ottawa samples*

sample	H_1(T)	H_2	$H^{\dagger}_{av}$	σ_1(mm/s)	σ_2	$\sigma^{\dagger}_{av}$	ε(mm/s)	CS(mm/s)
a)								
PBH	51.84		51.84	.029		.029	-.126	.348
G12	51.72	50.08	51.36	031	.113	.049	-.132	.348
G1	51.59	49.74	51.19	.035	.113	.052	-.131	.347
L9	51.55	49.46	51.00	.034	.108	.054	-.130	.348
M60	51.07	48.96	50.43	.035	.108	.056	-.129	.350
b)								
PBH	51.40		51.40	.026		.026	-.106	.368
G12	51.37	50.62	51.21	.027	.133	.050	-.110	.369
G1	51.12	50.11	50.86	.028	.153	.060	-.108	.370
L9	51.34	49.72	50.89	.025	.132	.054	-.108	.373
M60	50.82	48.79	50.24	.032	.124	.069	-.108	.370

*In these fits, the coupling parameters δ_1 and ε_1 were frozen to be zero. The height ratios R1(=h1/h3) and R2(=h2/h3) are constrained in 2.6 ~ 3 and 1.6 ~ 2, respectively. Also note that hyperfine fields H and HFD widths σ should have the same units, however, for convenience we give H in Tesla and σ in mm/s, where $g^*\mu_N H$ (in mm/s) = (6.757×10^{-2} mm/s per Tesla)·H (in Tesla).

Table 5.1.2 continued....

$h3_1$	$h3_2$	BG	$\gamma/2$	R1	R2	$A1/A_t^{**}$	reduced χ^2
108943		1290362	0.13	2.44	1.74	1.00	11.6
151662	40860	2047661	0.13	2.74	1.85	0.79	16.7
204707	56231	2729514	0.13	2.74	1.85	0.78	18.4
208730	72965	2881224	0.14	2.75	1.85	0.74	20.7
216811	95084	3728713	0.15	2.75	1.85	0.70	20.7
164722		1278672	0.14	2.20	1.70	1.00	34.3
39072	10739	433452	0.13	2.60	1.90	0.78	11.1
91671	31701	780600	0.12	2.60	1.91	0.74	31.7
41056	15611	373512	0.13	2.60	1.91	0.72	16.6
63448	25211	646471	0.14	2.60	1.91	0.70	17.4

a) Absorbers prepared in the first way and run outside the cryostat.

b) Absorbers prepared for low temperatures: first run at RT in the cryostat.

† H_{av} is the weighted average hyperfine field and σ_{av} is the weighted average HFD width.

** $A1/A_t$ is the fractional spectral area for the first HFD component.

going from PBH to M60 in the sequence of their impurity contents as listed in Table 5.1.2. The defect component is related to the impurities: the more non-Fe_2O_3 material in a sample, the more defect sites in the Fe_2O_3 material.

(C). As seen in Table 5.1.3, the averaged hyperfine fields for both PBH-like and defect components generally decrease with increasing impurity content. But in L9, its PBH-like field is higher than that of G1 in one experiment, while in the other it is not.

(D). The center shifts and the quadrupole splittings do not show obvious correlations to the impurity amount.

Other constraints were also tried in our fitting. Comparison of fit quality is given in Table 5.1.3. Our various fitting attempts demonstrate that the quadrupole splitting ε has at most a very weak coupling to the hyperfine field. It is therefore certainly the hyperfine field distribution, rather than the quadrupole splitting distribution, that broadens the spectra.

d. Fitting results for the L samples

The other four samples involved in this study are L1, L3, L7, and L10. They were synthesized in the same way as

Table 5.1.3 Comparison of different fits for RT Ottawa samples

constraint	sample	reduced χ^2 (a)	reduced χ^2 (b)	comment on results
1.	PBH		71.92	
	G12		14.32	big χ^2
$R1^{\dagger} = 3$	G1		41.44	for using
$R2^{\dagger} = 2$	L9		20.66	ideal height
	M60		23.36	ratios
			171.55	
2.	PBH	11.67		non-zero values
	G12	21.16		of ε_1 and δ_1
$2.6 < R1 < 3$	G1	18.13		allow trade-offs
$1.6 < R2 < 2$	L9	20.65		between fit
	M60	20.60		parameters
		92.21		
3.	PBH	16.38	71.82	
	G12	18.40	14.42	big χ^2
$R1 = 3$	G1	21.76	42.66	(two groups
$R2 = 2$	L9	23.14	21.40	have different
$\varepsilon_1 = \delta_1 = 0$	M60	21.94	23.89	absorber
		101.54	174.19	thicknesses)

Table 5.1.3 continued...

4.	PBH	11.64	45.32	
	G12	16.76	11.06	freezing δ_1
$\delta_1 = 0$	G1	18.09	32.87	does not affect
$2.6 < R1 < 3$	L9	20.63	16.22	the fit goodness
$1.6 < R2 < 2$	M60	20.62	18.14	ε_1 is about .01
		87.74	123.62	
5.				
	PBH	11.63	34.30	good fits
$\delta_1 = \varepsilon_1 = 0$	G12	16.77	11.12	but different R1's
$2.6 < R1 < 3$	G1	18.20	31.67	and R2's cause
$1.6 < R2 < 3$	L9	20.67	16.56	non-uniqueness of
	M60	20.58	17.44	the two component
		87.85	111.09	relative amounts
6.				
	PBH	11.08		
$\delta_1 = \varepsilon_1 = 0$	G12	16.07		
$R1 = 2.74$	G1	18.32		final fits*
$R2 = 1.85$	L9	20.61		
	M60	20.72		
		86.80		

(a). Samples mearsured in cryostat.

(b). Samples measured outside cryostat.

† R1 = h1/h3, R2 = h2/h3.

* In the final fits, R1 and R2 in PBH are free because it has only one HFD component.

L9, only the reaction temperature was different for each sample (Table 3.1.1).

The line widths for some of these L samples are much greater than in the Ottawa samples. Since the L samples contain a very broad range of the impurity content with the same synthesis method, the impurity effects and the correlations to the reaction conditions are easier to ascertain.

We use the same HFD approach to fit the spectra of the L samples with one "site" having two components in the HFD. The same constraints are imposed on the height ratios (R1 and R2 same for all L samples) and coupling parameters (δ_1 = ε_1 = 0) as in section 5.1.c. Here, however, the ratios obtained from fitting these spectra automatically reach the values of R1 = 3 and R2 = 2. This suggests that the CANMET absorbers were made with less material per unit area.

As mentioned in section 5.1.b, L1 and L3 were seen to have minor amounts of FeO.OH. This impurity six-line pattern distorted the spectra of L1 and L3 significantly. Therefore in fitting these two spectra, we assume the usual hematite one site with two distribution components plus another sextet component with parameters frozen at the known values for FeO.OH (Morup et al., 1983).

In the other L samples the impurities are negligible. Good fittings are readily obtained with a one-site

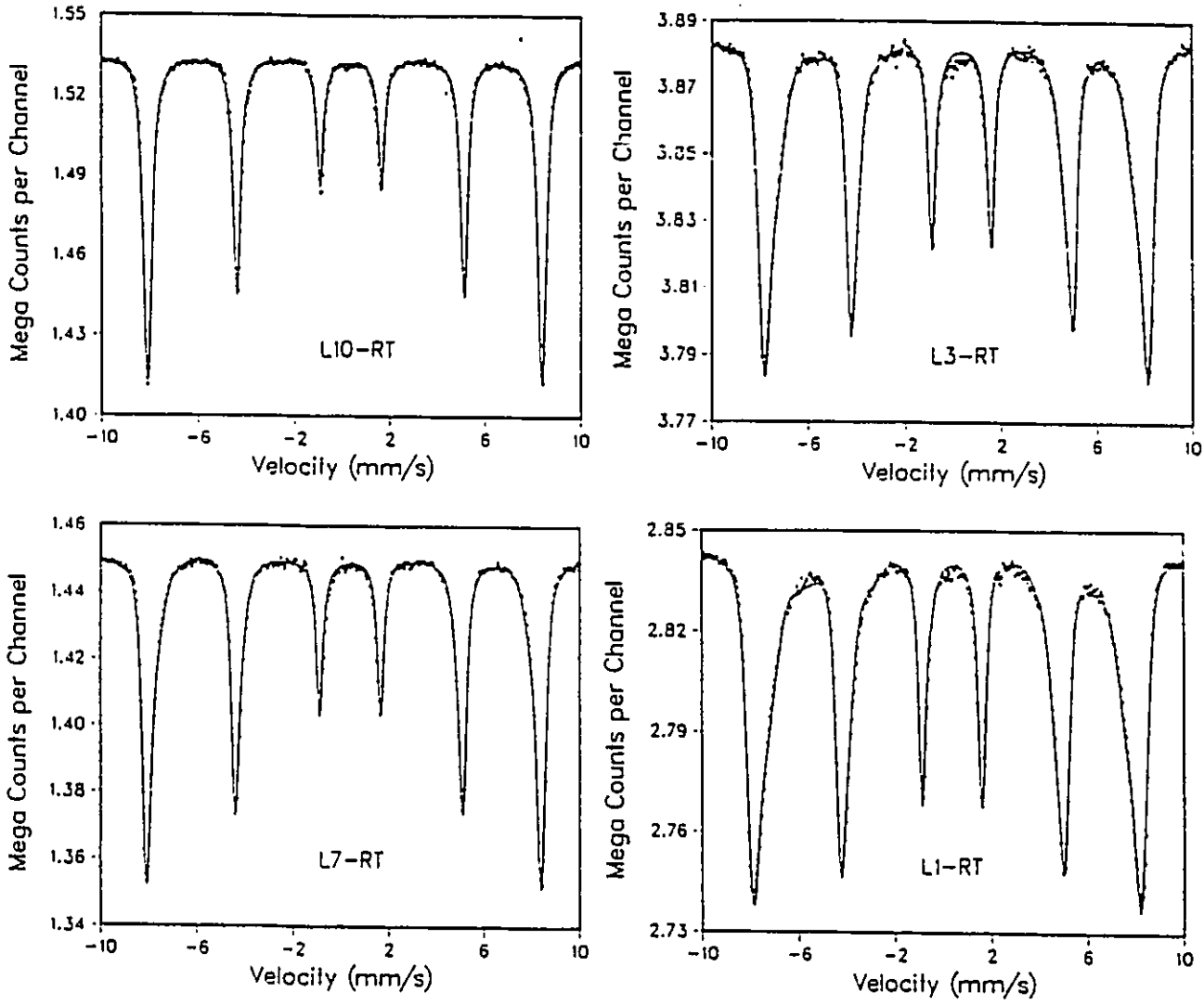

Fig.5.1.8 RT Mössbauer spectra of L samples fitted with a HFD having two assumed Gaussian components and corresponding to a single "site" (1-site/2-component model).
See Table 5.1.4 for corresponding fit parameters.

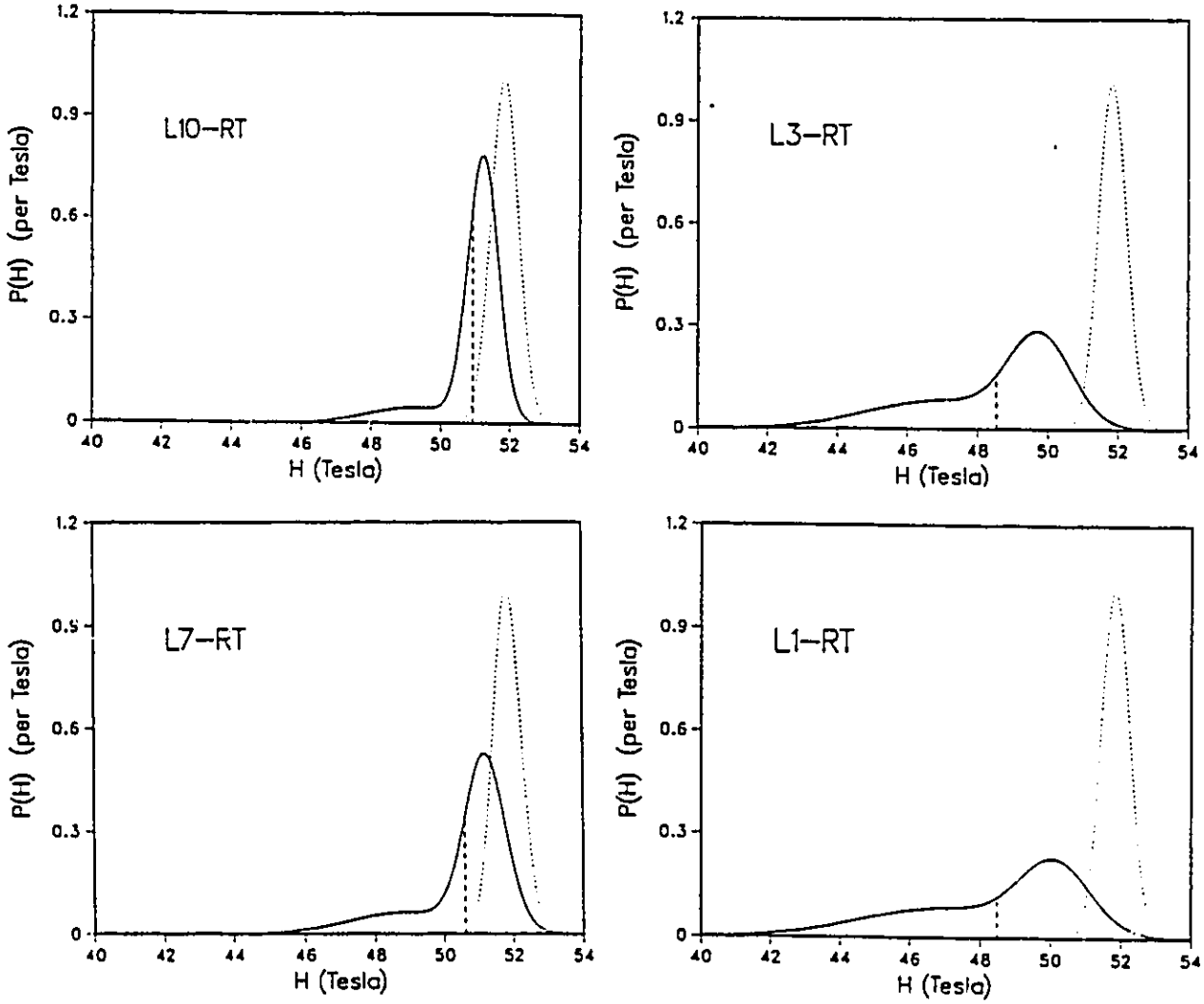

Fig.5.1.9 RT hyperfine field distributions of L samples corresponding to the single site with two Gaussian component fits.

Table 5.1.4 RT fit parameters for the L samples

sample	H_1(T)	H_2	$H^{\dagger}_{av}$	σ_1(mm/s)	σ_2	$\sigma^{\dagger}_{av}$	ε(mm/s)	CS(mm/s)
L10	51.23	49.23	50.93	.030	.088	.0386	-.102	.263
L7	51.14	48.92	50.60	.0400	.111	.0585	-.104	.261
L3	49.77	46.89	48.53	.0606	.140	.0906	-.095	.260
L1	50.12	46.91	48.47	.0672	.161	.1056	-.096	.262

Table 5.1.4 continued....

$h3^{*}_1$	$h3^{*}_2$	$h3^{**}$	BG	$\gamma/2$	h1/h3	h2/h3	$A1/A_t$	reduced χ^2
44212	7855		1534085	0.16	3	2	0.85	2.44
36008	12686		1450534	0.16	3	2	0.74	1.84
37058	27927	2898	3884192	0.18	3	2	0.55	1.13
39056	41176	7408	2843836	0.17	3	2	0.45	2.38

† H_{av} is the weighted average field.

σ_{av} is the weighted average HFD width. Note that hyperfine fields H and HFD widths σ should have the same units, however, for convenience we give H in Tesla and σ in mm/s, where $g^{*}\mu_N H$ (in mm/s) = $(6.757\times10^{-2}$mm/s per Tesla)·H (in Tesla).

* $h3_1$ is the inner line height for the first Gaussian component, $h3_2$ is the inner line height for the second component.

** h3 is the inner line height for the impurity FeO.OH sextet.

two-component HFD for hematite only.

The resulting fit parameters are listed in Table 5.1.4. The fitted spectra are given in Fig.5.1.8. The hyperfine field distributions corresponding to our one-site two-component model are shown in Fig.5.1.9 with that of PBH as a reference.

The results from the fitting of the L samples are consistent with what we get from the Ottawa samples. The two components of the distributions seen in Fig.5.1.9, the averaged hyperfine fields, and the distribution widths listed in Table 5.1.4, all change systematically with the known impurity contents of the samples.

The results obtained from the Ottawa and L samples are compared in Figs.5.1.10, 5.1.11, and 5.1.12.

Fig.5.1.10 shows the fraction of the PBH-like component as a function of sample purity for all the samples. It suggests that in our hematites iron ions in the PBH-like component of the HFD are related to the overall sample purity, irrespective of how the samples were synthesized, and of what particular impurities they contain in various relative amounts.

Fig.5.1.11 shows the hyperfine fields for the PBH-like and defect components as functions of sample purity, and also the average hyperfine field as a functions of sample purity. Fig.5.1.12 shows the HFD widths as functions of the

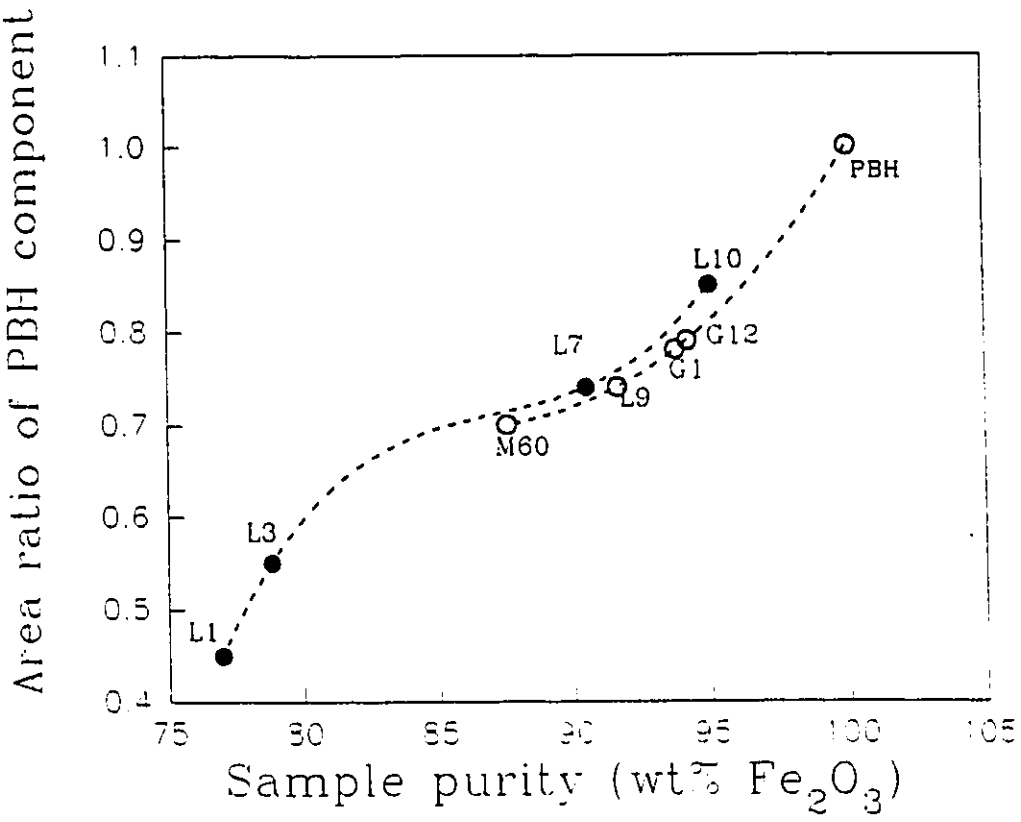

Fig.5.1.10 RT spectral area fraction of PBH-like componentas a function of the corrected (Table 5.1.1) sample purity for Ottawa and L samples.

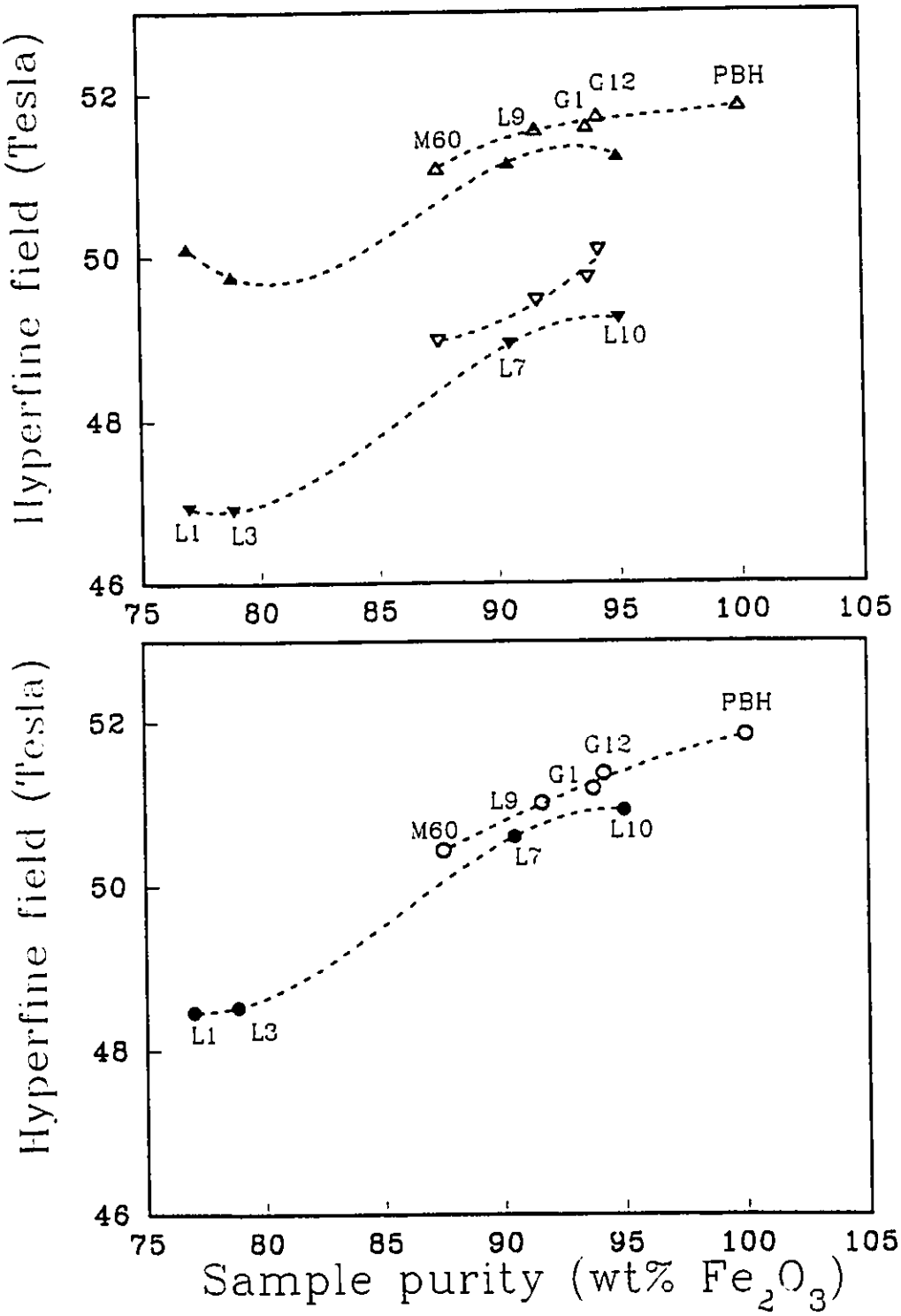

Fig.5.1.11 RT component-specific hyperfine fields (top) for the PBH-like (upper pointing triangles) and the defect (downward pointing triangles) components and the component-wise average hyperfine fields (bottom), all as functions of the corrected (Table 5.1.1) sample purity.

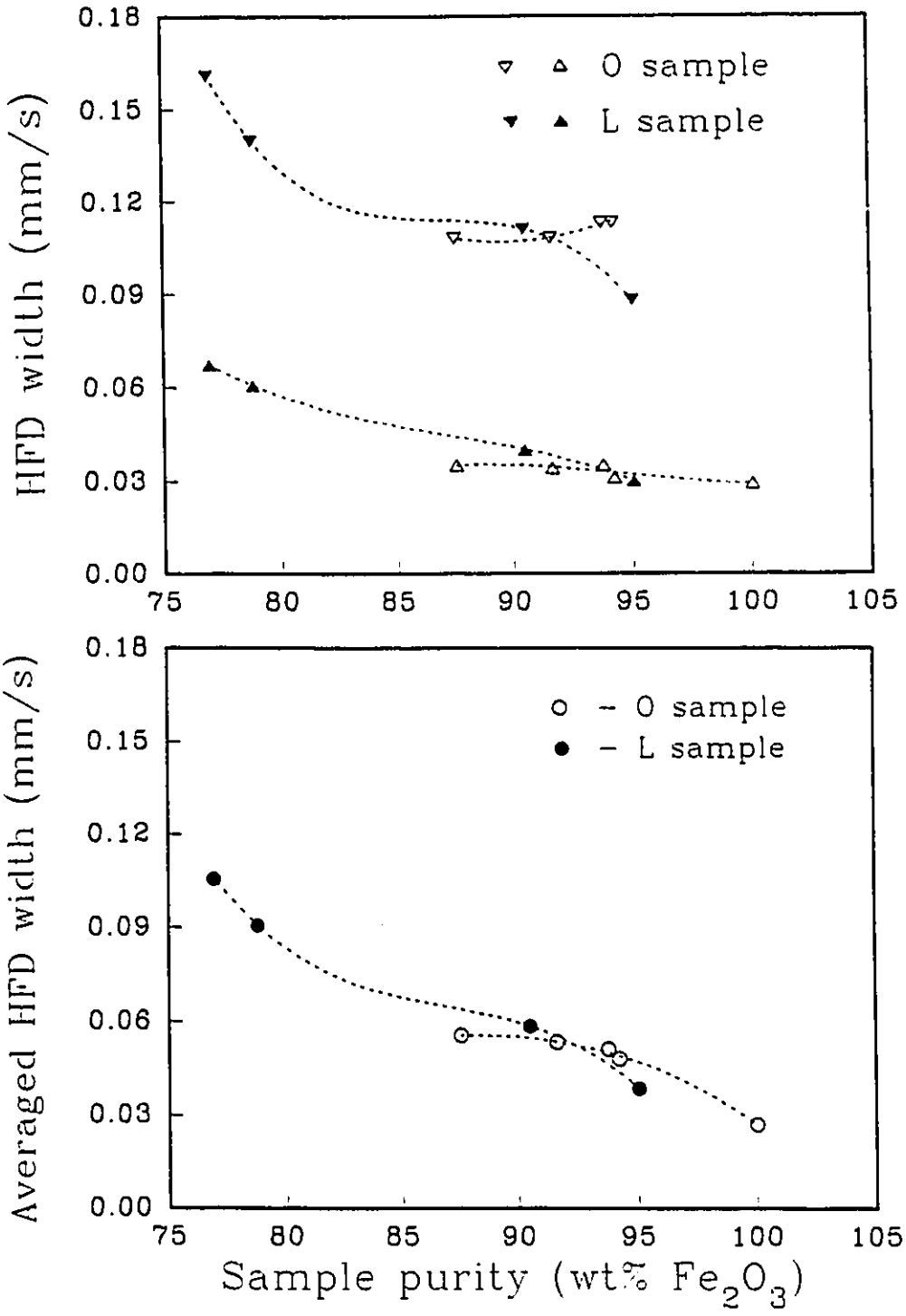

Fig.5.1.12 (a) RT component specific HFD widths (top) and the components-wise average HFD widths (bottom) as functions of the corrected sample purity.

sample purity. It is clear that relatively pure samples have larger hyperfine fields and smaller HFD widths.

In summary, many physical properties show systematic changes with overall sample purity (wt% Fe_2O_3). It can be concluded that the less non-hematite material is in a sample, the less defects are present in the hematite, the higher the crystal quality of the hematite, the larger the hyperfine fields in the hematite, and the narrower the HFD's. All of these properties are correlated via the overall sample purity which exhibits itself as a "good" characterization parameter and have a common cause: the synthesis conditions.

For example, in the L samples, the sample purity (i.e wt% Fe_2O_3) is directly related to the reaction temperature during syntheses. This is illustrated in Fig.5.1.13.

The spectral line broadening at RT is due to hyperfine field distributions resulting from defects (i.e. surface and vacancies) in the hematite material. The defect densities in the hematites and the overall amounts of all the impurities in the samples are both caused by the synthesis conditions.

We conclude that several key spectral features are presumably caused by similar intra-hematite defects and are thereby correlated to each other. Since the intra-hematite defect density is related to resultant hematite content of a

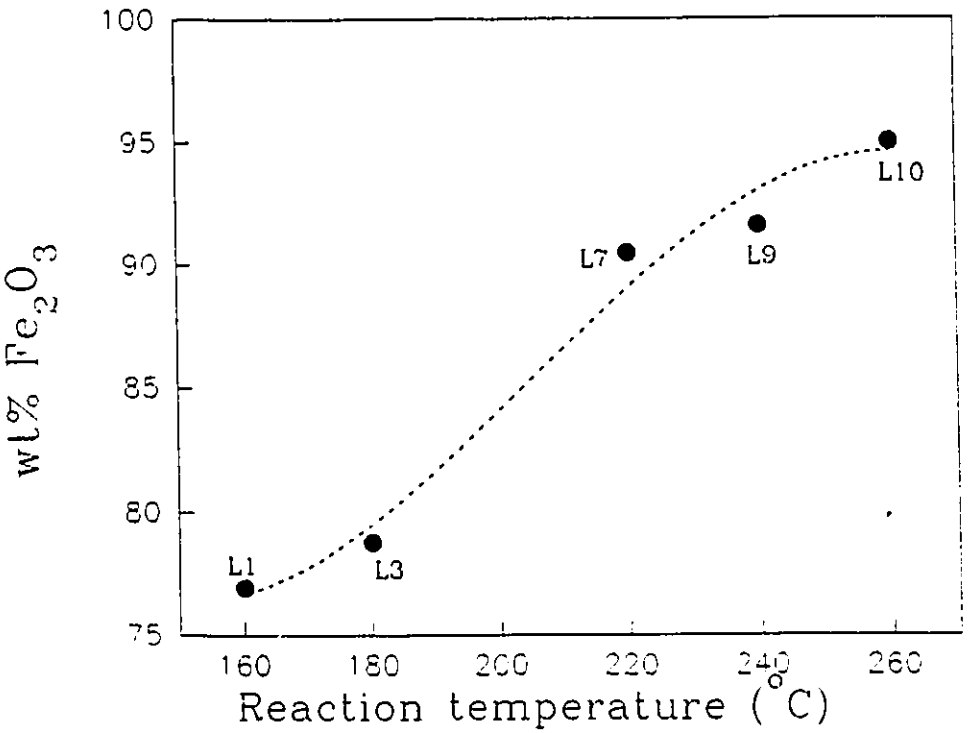

Fig.5.1.13 Corrected (Table 5.1.1) sample purity (or hematite yield or wt% Fe_2O_3) as a function of reaction temperature for the L samples.

given sample via the synthesis conditions (i.e. hematite yield and hematite quality are expected to be strongly correlated), the sample purity (wt% Fe_2O_3) reveals itself as a good parameter for studying the systematics of the spectral characteristics.

5.2 Low Temperature Behavior (LT ≃ 80K)

a. Morin transition in Mössbauer spectra

The Morin transition can be readily recognized by Mössbauer spectroscopy because the hyperfine field direction is collinear to the spin direction. The change of the spin direction is reflected in the quadrupole splitting shift ε (section 2.3 and Fig.2.3.1):

$$\varepsilon = \frac{e^2qQ}{4}[1 - \frac{1}{2}(3-\eta\cos2\phi)\sin^2\theta] \qquad (5.2.1)$$

where eq is the principal component of the electronic electric field gradient (efg) at the nucleus, eQ is the nuclear quadrupole moment of the first excited state, η is the asymmetry parameter of the efg, θ and ϕ are the polar and azimuthal angles respectively of the hyperfine field direction relative to the principal axes of the efg tensor (see Greenwood and Gibb, 1971). Equation 5.2.1 assumes that the efg term is much smaller than the hyperfine splitting term (Zeeman term) and is obtained by pertubation theory.

In pure bulk hematite, η is zero, and the [111] axis direction is the efg principal axis (Van der Woude, 1966). Therefore, when spins go from the WF state ($\theta \simeq \pi/2$, see section 2.2) to the AF state ($\theta \simeq 0$), the quadrupole

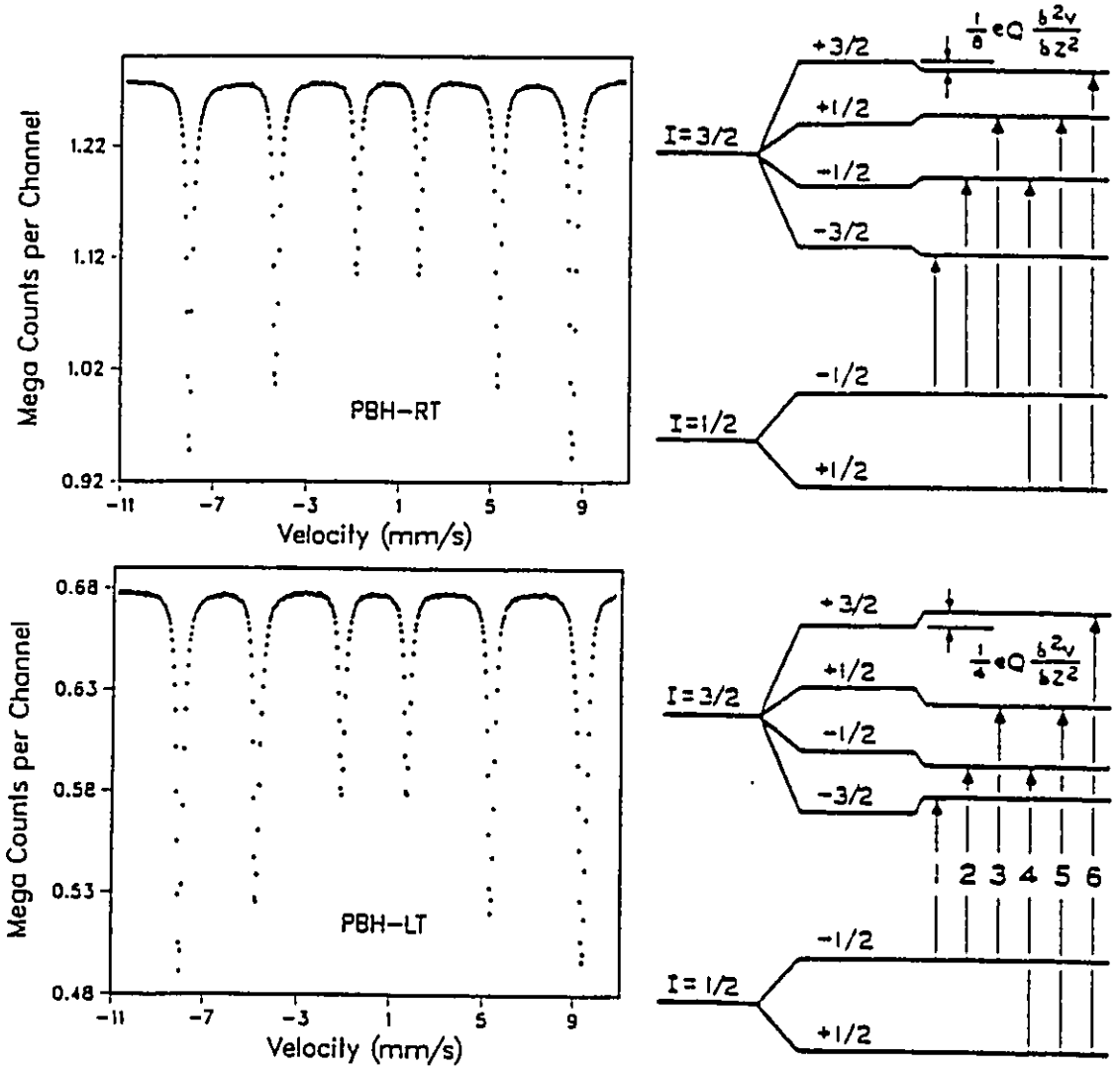

Fig.5.2.1 Mössbauer spectra of PBH at RT (above the Morin transition; WF state spin structure) and LT (below the Morin transition; AF state spin structure) and the corresponding Fe-57 energy level diagrams.

splitting shift ε changes sign and doubles in magnitude. Also, the hyperfine field drops by about 8 kOe because the net dipole-dipole fields at all sites are different (Van der Woude et al., 1966).

Fig.5.2.1 shows the spectra of PBH at both RT and LT, and the energy level diagrams corresponding to the relevant γ-ray transitions.

An important question is now: "if no Morin transition occurred in the sample down to LT, then what would the spectrum of the WF state at LT in PBH look like?" Simulation can answer this question.

A program called MAQUAD (Rancourt et al., 1985b) was first used to fit the LT spectrum of PBH to get the parameters of the AF state at this temperature. This program calculates line positions and intensities exactly, without assuming that e^2qQ is a small perturbation on the Zeeman splitting $g^*\mu_N H$. The resulting fit parameters were used in the simulation except that θ was taken to be $\pi/2$ instead of $\theta = 0$, i.e. we force the spins to stay near the (111) plane, and do not allow the flip that would occur at T_M. Then, considering that differences between the states at low temperature (i.e. the true low temperature AF state and the simulated low temperature WF state) are not only in θ but also in the magnitude of the hyperfine field due to the dipole-dipole interaction, we make the above mentioned 8

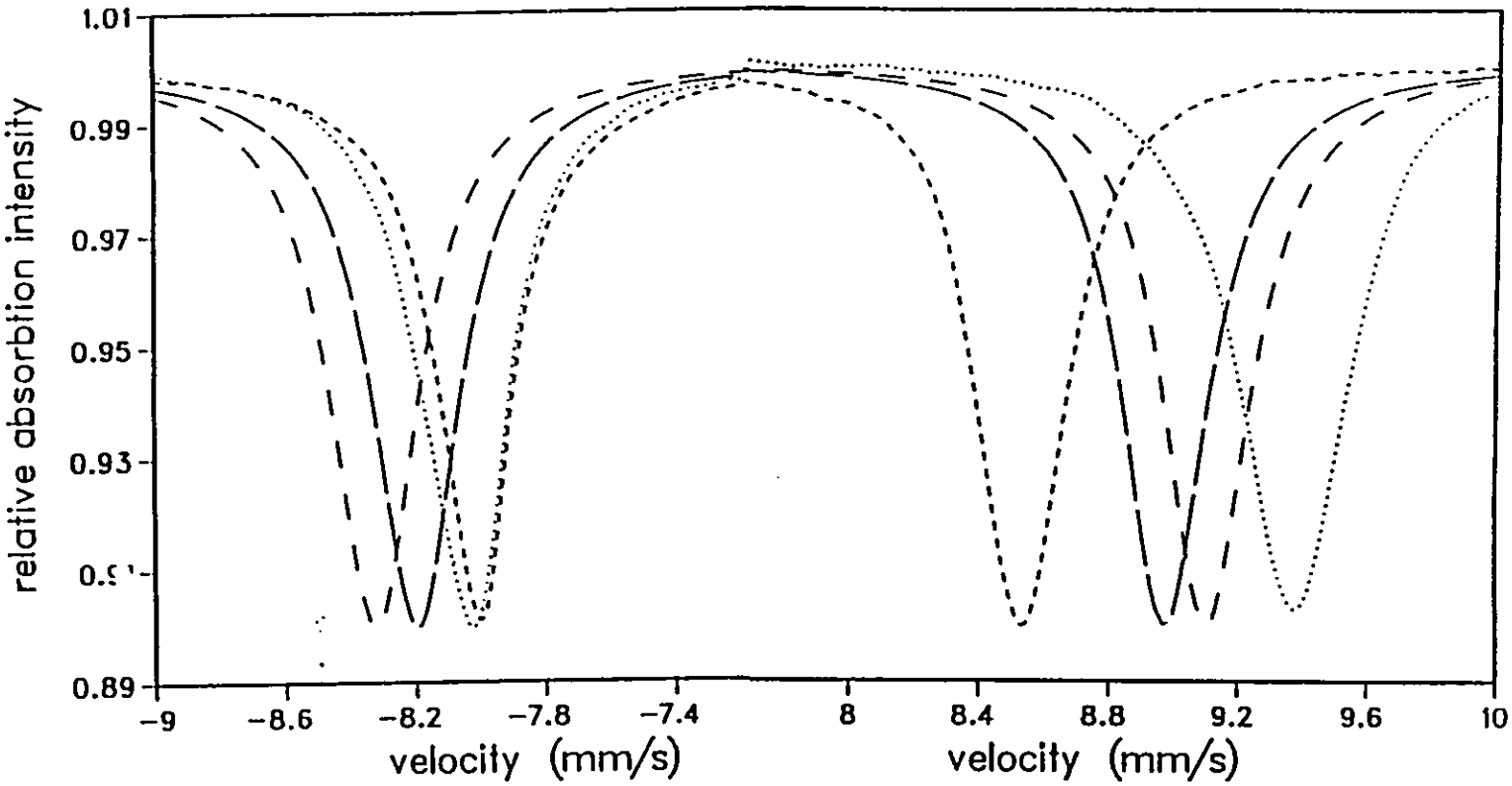

Fig.5.2.2 Line-1 and line-6 for both PBH spectra at RT and LT and the simulated spectrum of WF-LT with and without the 8 KOe dipole-dipole correction.

- - - - PBH RT, ... PBH LT.

-- -- -- -- simulated WF-LT without 8 KOe correction.

--- --- --- simulated WF-LT with 8 KOe correction.

KOe correction to the hyperfine field.

The simulation produces a new spectrum truly representing the WF state at LT as it would arise at LT. Lines 1 and 6 of both the simulated spectrum and the actual RT and LT spectra of PBH are shown in Fig.5.2.2. Lines 1 and 6 of the simulated spectrum without the 8 KOe dipole-dipole field correction are also shown.

In fact, however, the Morin-like transitions in small particle and impure hematites are more complicated. The WF and AF states, the Morin transition temperature T_M, the transition width ΔT_M and the microscopic details of the reorientation itself are all affected by the sample characteristics. We describe this for our samples in the next section.

b. LT spectra for the Ottawa samples

Mössbauer experiments were carried out at liquid nitrogen temperature (LT) on the Ottawa samples from PBH to M60.

The spectra at LT are shown in Fig.5.2.3. Systematic changes occur that are most obvious in line-6. Its line width, relative depth, and position all change from sample to sample. Fig.5.2.4 shows line-1 and Line-6 for the

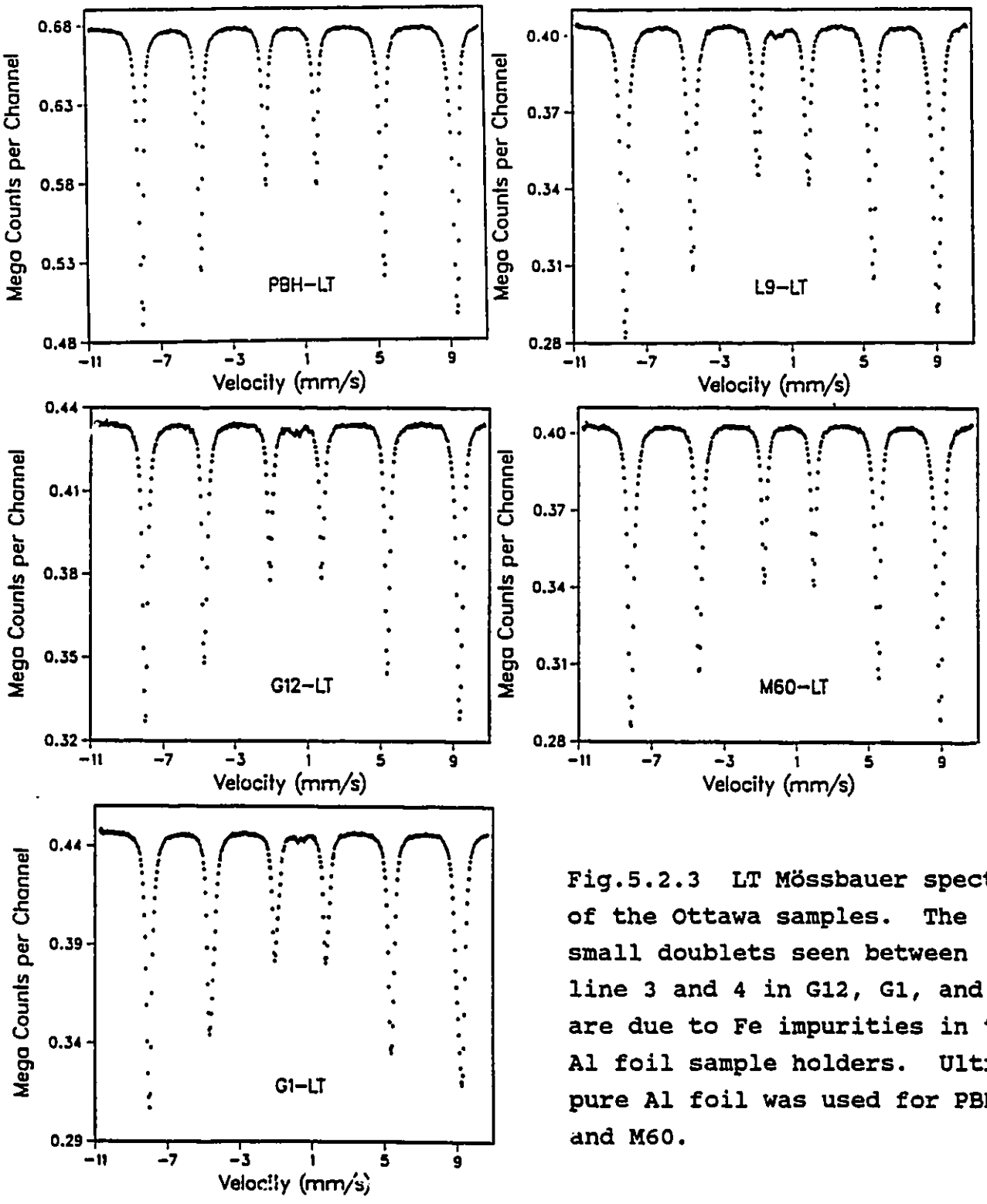

Fig.5.2.3 LT Mössbauer spectra of the Ottawa samples. The small doublets seen between line 3 and 4 in G12, G1, and L9 are due to Fe impurities in the Al foil sample holders. Ultra-pure Al foil was used for PBH and M60.

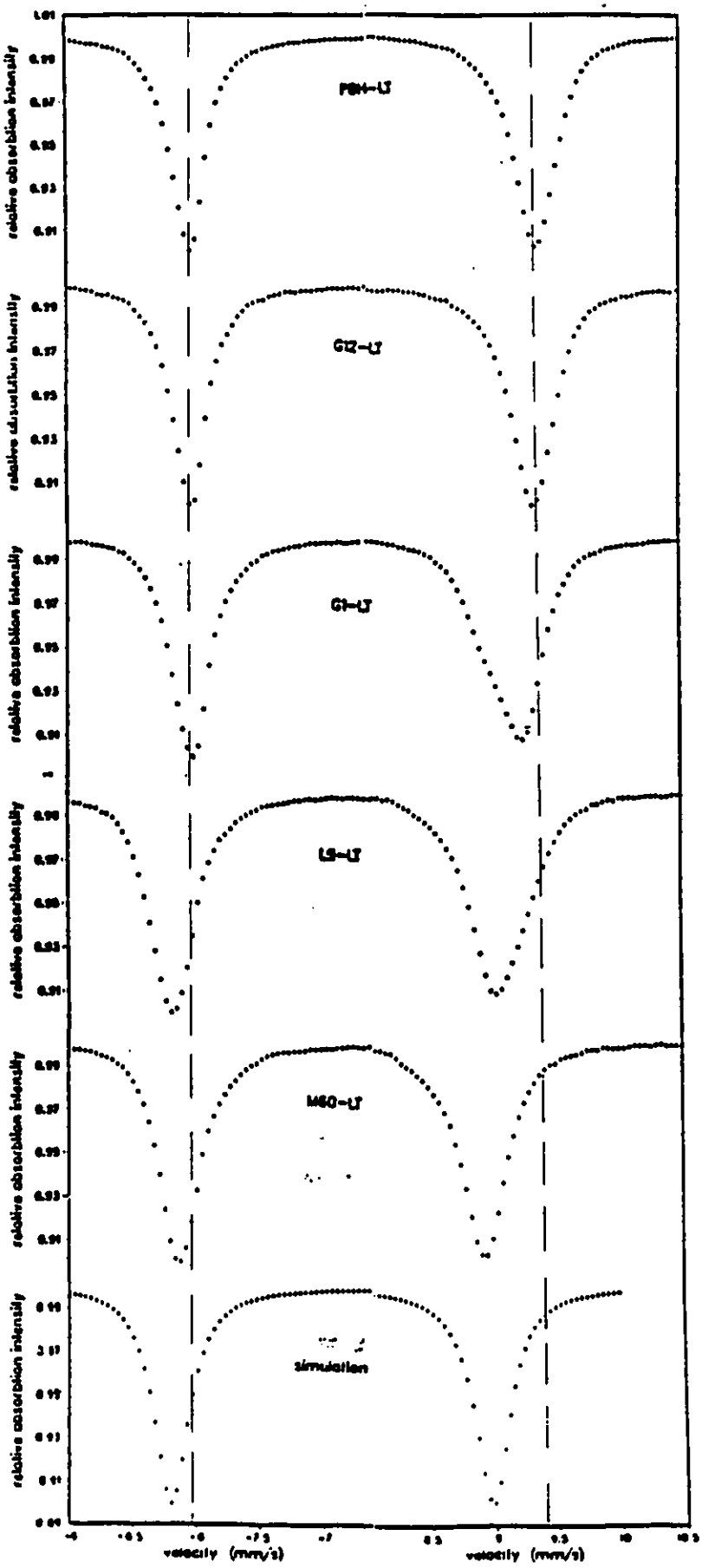

Fig.5.2.4 Line-1 and line-6 from LT spectra of Ottawa samples and the simulation of WF-LT state for PBH.

spectra at LT and the simulated spectrum for the WF state at LT.

As seen in Figs.5.2.3 and 5.2.4, line-6 has the same height as line-1 in PBH. We say that this spectrum is "symmetric". The spectrum of G12 has almost the same symmetry as PBH. But in the spectra of G1 and L9, line-6 becomes shallower and broader than line-1. For M60, however, the spectrum is back to being symmetric again.

To give a better view of what is happening at LT, Fig.5.2.5 gives line-1 and line-6 for the spectra at both RT and LT. On comparing the spectra at both RT and LT, the Morin transition behavior can be recognized.

Fig.5.2.5 indicates that the progressive sample to sample changes in the spectra result from differences in the Morin transition.

Two states seem to exist in our samples at low temperatures. One corresponds to a PBH-like state that has undergone the Morin transition at LT. The other, corresponds to the state in M60 that has had no Morin transition down to LT. These two states are present in relative amounts that vary systematically in the sequence of the sample purity.

These two states are explored further by fitting the spectra.

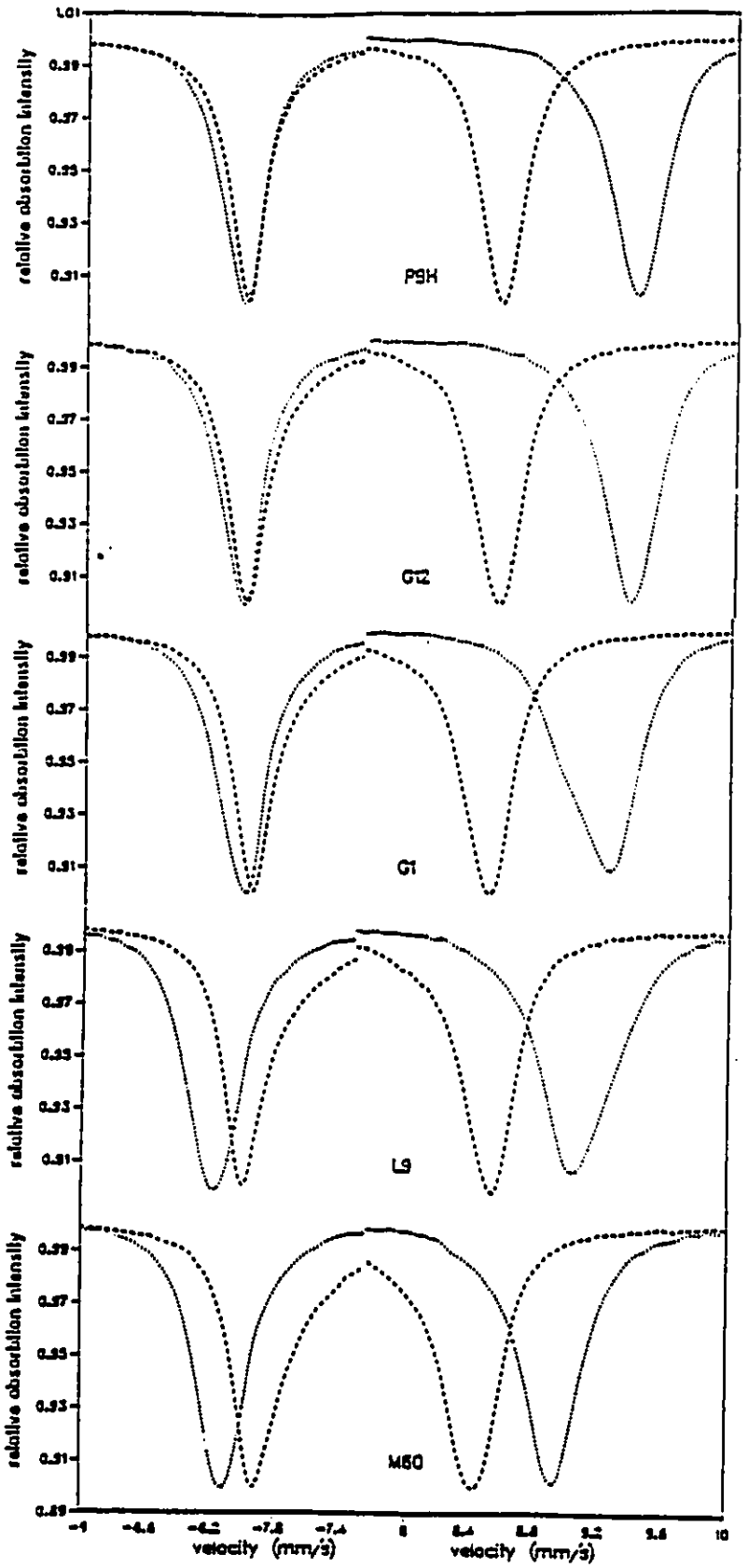

Fig.5.2.5 Line-1 and line-6 from RT and LT spectra of Ottawa samples.

c. Fitting with PBH-like AF and PBH-like WF states

Two site HFD's are used to model the two states that coexist in the LT spectra. Each site is supposed to have one Gaussian component in its HFD.

Two state coexistence has been assumed by other authors (e.g. De Grave et al., 1983, 1990) to explain Al-substituted bulk hematite spectra at LT. Usually, the two states are assumed to be the bulk-like AF and the WF state. Similarly, our first fitting model is to use the PBH AF and WF state spectra as subspectra to fit our spectra. Fitting PBH with one site only can produce the parameters of the AF state at LT. The WF state parameters are obtained from the simulation described in section 5.2.a.

With this first model, the two subspectra have fixed line positions since frozen assumed values of hyperfine fields (z_o), center shifts (CS = δ_o; δ_1= 0), and quadrupole splittings ($\varepsilon = \varepsilon_o$; ε_1= 0), corresponding to the assumed PBH AF and WF states, are used. The other parameters, including the height ratios (R1 and R2), the distribution widths (σ_z), and the Lorentzian width γ are left as free fitting parameters.

The LT spectrum of G1 has the most obvious coexistence of two states. Its line-o is very broad and has a distinctive bi-model structure, see Fig.5.2.4. It is used

to illustrate the inadequacy of our first model in Fig.5.2.6 (top). The fit parameters for this and other simple models for sample G1, are given in Table 5.2.1.

This model is clearly overly simple. It does not correctly describe the true LT states of the samples. Nevertheless, it was important to demonstrate this and establish that our samples cannot simply be viewed as a mixture of regions that have or have not undergone Morin transitions at LT.

Since the 8 kOe correction used in deriving our LT-WF simulation (section 5.2.a) arises from dipole-dipole effects and since such dipole-dipole effects are potentially sensitive to particle shape and intra-domain magnetization density, it makes sense to extend our first model to a second model in which we allow the two hyperfine field distribution centers (z_{OAF} and z_{OWF}) to be free parameters.

The resulting fit to the LT spectrum of G1 is shown in Fig.5.2.6 (bottom). Its fitting parameters are also listed in Table 5.2.1. The failure of this second model (Fig.5.2.6 (bottom) shows that states having the quadrupole splittings (ε_{AF-LT}= 0.185 mm/s and ε_{WF-LT} = -0.0925 mm/s) of ideal AF and WF LT states cannot be used to model the true LT states of our samples. We must acknowledge that the material is different enough from PBH to have hyperfine electric field gradient (efg) parameters (e^2qQ and η) and/or relative spin

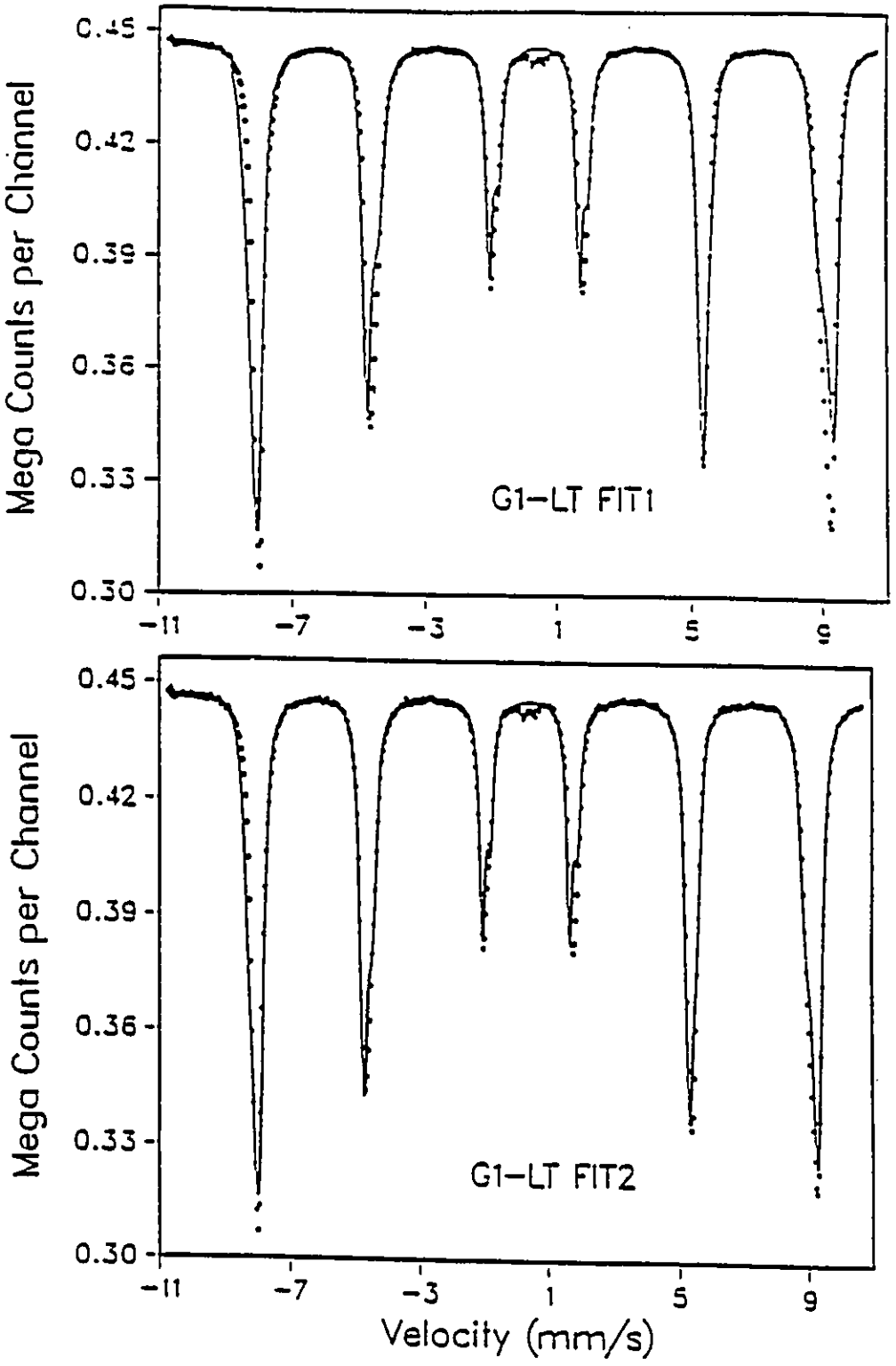

Fig.5.2.6 (Fit1) Fitted Mössbauer spectrum of G1 using two assumed subspectra with frozen z, ε, δ values corresponding to: PBH AF-LT state and simulated PBH WF-LT state. (Fit2) Fitted Mössbauer spectrum for G1: same as Fit1 except that the hyperfine splitting z of the two states are free parameters.

Table 5.2.1 Fitting parameters for G1 at LT: three overly simple models

trial	state	H(T)	σ(mm/s)	ε(mm/s)	CS(mm/s)	R1*	R2*	h3*	χ^2_{red}
Fit1	AF-PBH	54.10	0.041*	0.184	0.482	2.0	1.74	59363	161
	WF-PBH	53.36	0.079*	-0.093	0.482	3.0	1.79	31035	
Fit2	AF-PBH	53.59*	0.032*	0.184	0.482	2.2	1.79	58477	60
	WF-PBH	53.29*	0.044*	-0.093	0.482	2.4	1.69	31637	
Fit3	AF-PBH	54.10	0.037	0.184	0.482	2.1	1.74	54143	174
	WF-M60	52.96	0.039	-0.085	0.483	2.5	1.61	25707	

* These parameters are left free in the fitting, others are all frozen. Note that hyperfine fields H and HFD widths σ should have the same units, however, for convenience we give H in Tesla and σ in mm/s, where $g^*\mu_N H$ (in mm/s) = (6.757×10^{-2} mm/s per Tesla)·H (in Tesla).

and efg directions (θ and ϕ in Eq.5.2.1) that are significantly different from those of PBH, at most of the iron sites. Nonetheless, it is worthwhile pursuing a two-state picture somewhat further.

d. Fitting with a PBH-like-phase AF state and a defect-phase WF-like state

Rather than assume that both states are PBH-like states (with allowed and suppressed Morin transitions), we can assume that only the state with an allowed Morin transition is PBH-like and that the other state is some "defect-phase state" that has a WF-like rather than AF-like spin structure at LT.

Fig.5.2.4 suggests that we use the LT spectrum of M60 to represent the subspectrum of the defect-state in the other samples at LT. The PBH-like state is represented by the PBH spectrum. Line positions are frozen at these PBH and M60 values as in the first model described above (values of σ_H, R1, R2 and $\gamma/2$ are free). The resulting fit for G1 is shown in Fig.5.2.7, and the corresponding fit parameters are again given in Table 5.2.1.

Again, the fits are not acceptable. The M60 spectrum is

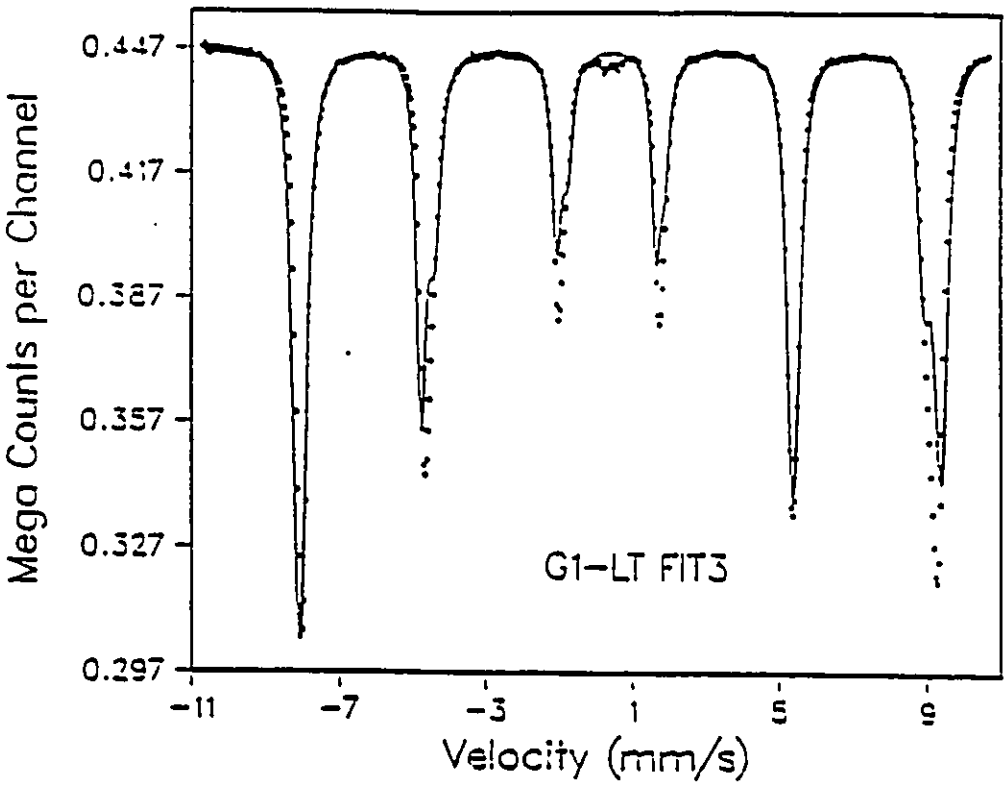

Fig.5.2.7 Fitted spectrum for G1: with hyperfine parameters z, ε, δ frozen at values corresponding to the PBH and M60 states at LT.

not representative of the defect-states in other samples or the true PBH parameters are not representative of the PBH-like states in the samples or both. We therefore next allow the spectral parameters to be significantly different from those of PBH or M60 and to be different from sample to sample.

Our final fits impose only a few restrictions: the height ratios are constrained as $2.6 < R1 < 3$ and $1.6 < R2 < 2$ and the center shifts are taken to have the values of PBH and M60 for the PBH-like states and the defect-state, respectively. The fitted spectra are shown in Fig.5.2.8, and the corresponding parameters are listed in Table 5.2.2.

From these fitting parameters, it is seen that the two states do change from sample to sample but they also retain their expected main characteristics: the PBH-like state has a higher field and bigger quadrupole splitting (close to the quadrupole splitting of PBH at LT) and the defect-state has a lower field and smaller quadrupole splitting (close to that of M60 at LT or PBH at RT). We take this last model as the simplest two-state model that is in satisfactory agreement with the data — the other models were not.

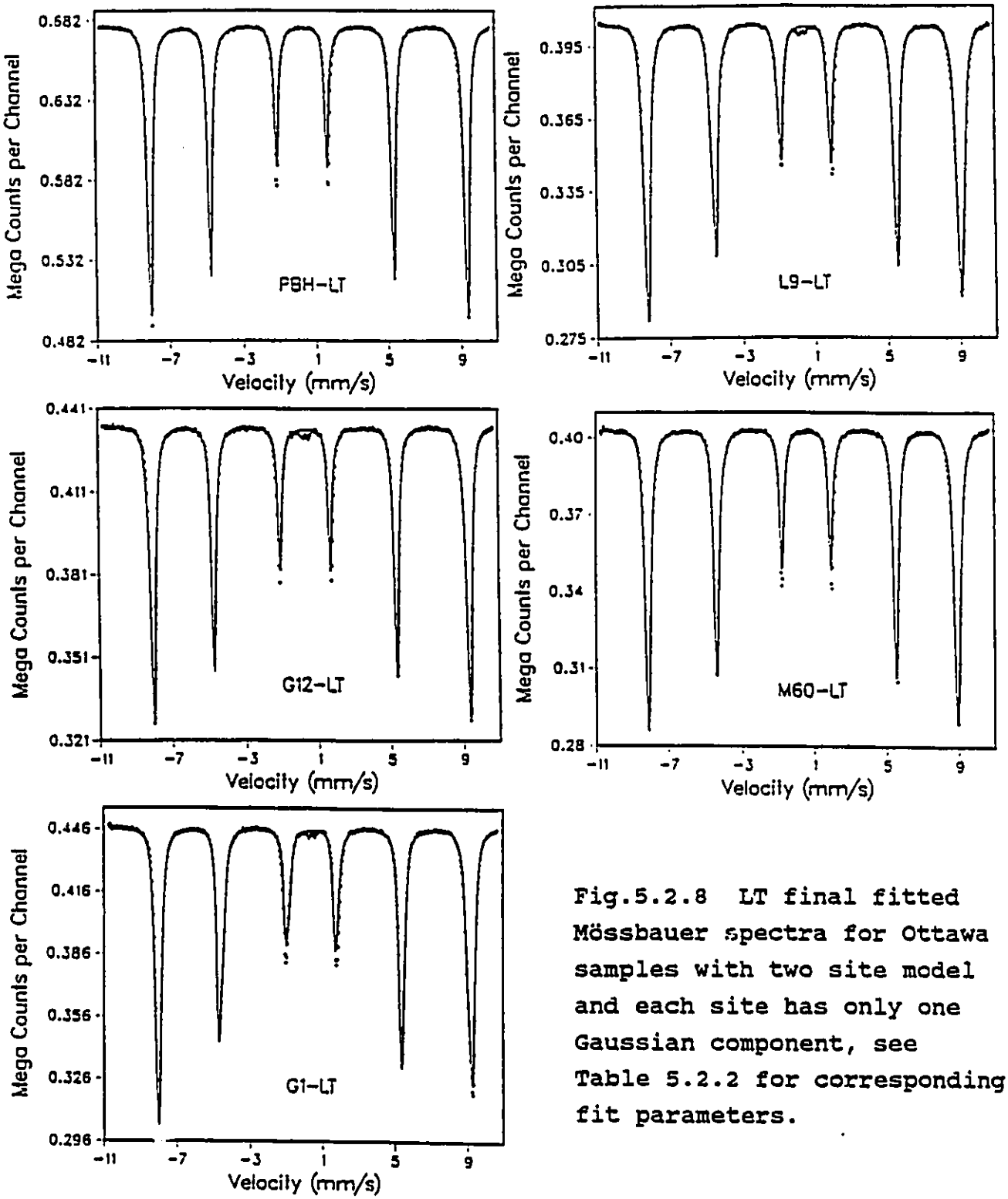

Fig.5.2.8 LT final fitted Mössbauer spectra for Ottawa samples with two site model and each site has only one Gaussian component, see Table 5.2.2 for corresponding fit parameters.

Table 5.2.2 LT Mössbauer fit parameters from 2-site fitting*

sample	H_1(T)	H_2	σ_1(mm/s)	σ_2	ε_1(mm/s)	ε_2	CS_1(mm/s)	CS_2
PBH	54.10		.037		.184		.482	
G12	54.03	53.86	.027	.084	.183	.097	.482	.483
G1	53.64	53.21	.033	.050	.157	-.019	.482	.483
L9	53.98	53.50	.018	.046	.111	-.073	.482	.483
M60		52.96		.039		-.085		.483

Table 5.2.2 continued....

$h3_1$	$h3_2$	BG	$\gamma/2$	h1/h3	h2/h3	$A1/A_t$	reduced χ^2
89268		678492	.14	2.60	1.96	1.00	29.5
40477	14548	434521	.14	2.60	2.00 1.60	0.74	14.1
46958	28039	446962	.13	2.60	2.00 1.83	0.63	23.8
9967	53309	404245	.15	2.60	2.00 1.89	0.16	15.1
55719		403804	.15	2.60	1.91	0.00	15.8

* In the fitting, coupling parameters δ_1 and ε_1 are frozen at zero. The height ratios are constrainted as 2.6<R1<3 and 1.6<R2<2. The CS_1 is frozen at CS of PBH, and CS_2 is frozen at CS of M60 when fitting the spectra of G12, G1 and L9.

e. Comparison of LT Mössbauer to other sample characteristics

The ratio of the PBH-like subspectral area to the total spectral area at LT is calculated from the fit parameters (Table 5.2.2) and is plotted as a function of corrected sample purity in Fig.5.2.9. This graph shows that the fraction at LT of hematite iron in PBH-like regions is directly related to the overall sample purity. Chemically impure samples have smaller fractions of their hematite that is PBH-like at LT than relatively pure samples.

Relatively pure samples also have higher degrees of effective crystal quality (section 3.3) and less defect sites as seen in their RT spectra (section 5.1.c). This strongly suggests that it is the higher quality hematite in a given sample that behaves PBH-like on going from RT to LT and, conversely, that the lower quality hematite in a given sample gives rise to the LT WF-like defect-state that does not undergo a Morin transition on going from RT to LT.

As pointed out in section 5.1, the fact that chemical purity (wt% Fe_2O_3) is a valid parameter for showing the above correlations between RT Mössbauer behavior, LT Mössbauer behavior, and effective XRD crystal quality, may simply be due to both the overall sample purity and the intra-sample hematite quality having common causes: the

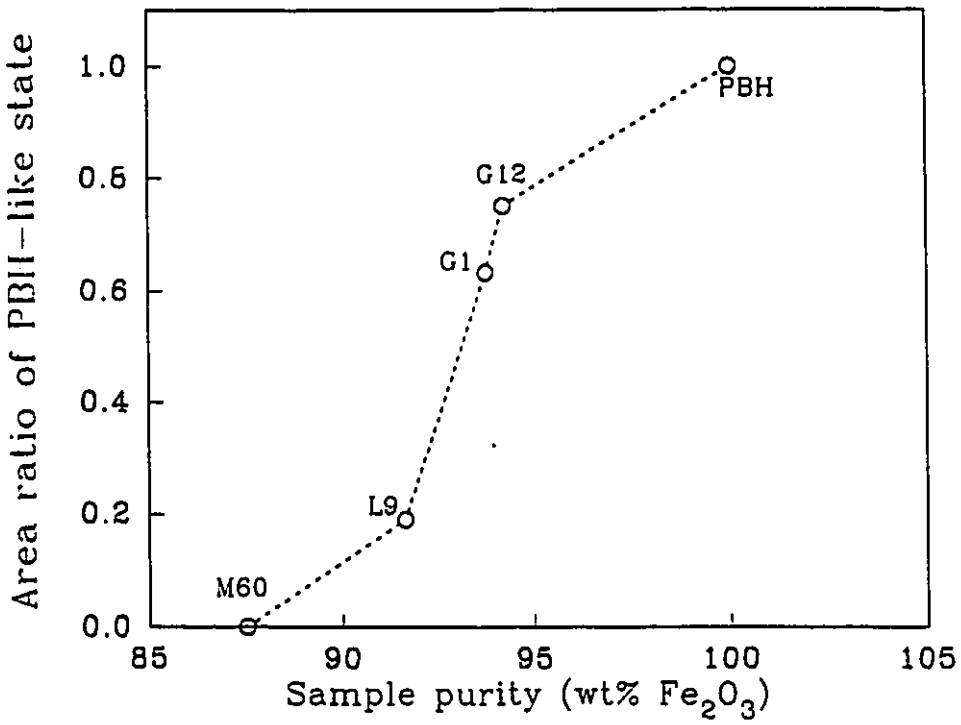

Fig.5.2.9 LT spectral area fraction for the PBH-like AF state as a function of sample purity for the Ottawa samples. This fraction corresponds to the fraction of the iron that has undergone the Morin transition.

synthesis conditions.

In other words, the impurities probably do not cause the observed properties directly. This is supported by the fact that only the net sample purity (or amount of hematite produced) seems to matter, rather than amounts of various impurities that can be identified ($FeSO_4$, FeO.OH, $Fe_2(SO_4)_3.nH_2O$ and H_2O). Simple impurity indicators such as wt% SO_4 and wt% δ (section 5.1.a) do not correlate with the observed properties of the intra-sample hematite. The relative amounts of quite different residual impurities seem to have no impact on the observed hematite properties.

These considerations strongly suggest that the sulphur does not incorporate the hematite structure in any of the samples studied. Within detection limits, all of the sulphur may go into such impurities as $Fe(SO_4).OH$ and $Fe_2(SO_4)_3.nH_2O$ ($n \propto 9\text{-}11$).

In comparing the LT and RT Mössbauer results, one must be wary not to directly associate the low-field HFD component seen at RT (section 5.1.c) with the WF-like defect-state seen at LT.

At RT all of the hematite in a given sample is in an essentially WF state. This is clear from Table 5.1.2 where the ε's at RT are seen to have the PBH value for all Ottawa samples. This is also true of the L samples (Table 5.1.4).

Such a sample independent PBH value of the quadrupole

splittings (ε in Eq.5.2.1) has several important implications. (i) Since $\eta \simeq 0$ in PBH, it must also be near-zero at most or all of the sites in our hematites. (ii) Since $\theta \simeq \pi/2$ in PBH at RT, most or all of the spins in our hematites must also be essentially in the (111) plane at RT (within ~ 2° - 3°). (iii) The efg magnitude q (and principal axis direction) must be the same at most or all of the sites in our samples as in PBH.

The only way that the above points (i-iii) can be incorrect is in the very unlikely situation where the different terms in Eq.5.2.1 would conspire to be different than in PBH in such a way that ε remains the same as in PBH — for all the samples.

At RT, therefore, the low-field HFD component corresponds to essentially WF state spins that have lower thermal average local moments. (Recall the relationship between hyperfine fields and average local moments in section 2.4) Such lower moments will occur at the surface of magnetic materials and do propagate to some depth within the material. Relatively large microcrystalline lattice expansion from locally higher densities of defects can also cause smaller average moments via smaller exchange constants. Magnetic exchange constants can be very sensitive to lattice spacing changes even for spacing changes that do not significantly affect hyperfine efg

parameters.

When the temperature is lowered, all such differences in local degree of magnetic order will be greatly reduced, by the same mechanism that allows different materials to have different ordering temperatures and similar saturation magnetizations. Low-field components are essentially not seen at LT where single-Gaussian HFD's (one for each state) are sufficient to fit the spectra (section 5.2.d).

The dominant feature at LT is whether or not a Morin transition has occurred. That is, whether the material (or part of the sample) has remained in an essentially WF state or has changed to an essentially AF state. We expect that most (if not all) of the RT defect component is in the LT WF-like state. In M60 all of the RT defect has to be in the WF-like state since only the latter state is populated at LT in this sample. In other samples it is possible that some relatively small fraction of the RT low field component is in the LT AF-like state.

Since most (when not all) of the RT defect component material contributes to the LT WF-like state contribution, a significant fraction of the RT PBH-like component material does not undergo a Morin transition on going RT -> LT ($\simeq$ 80 K) and thereby contributes to the LT WF-like component rather than to the LT AF-like component as would be expected of PBH-like material. This shows that relatively minor

defects (i.e. that only slightly affect the RT spectra) can effectively inhibit the Morin transition down to LT = 80 K.

f. Spin orientation at low temperature (80 K)

Spin orientation is related to quadrupole splitting by Eq.5.2.1 (see above):

$$\varepsilon = \frac{e^2qQ}{4}[1 - \frac{1}{2}(3-\eta\cos 2\phi)\sin^2\theta]$$

and is obtained via the hyperfine angles θ and ϕ. In PBH, η is zero such that the direction of the spin orientation is given only by θ. From ε it is easy to know the spin orientation in PBH. In impure hematites, defects may cause non-zero η's and then, it is problematic to know the spin orientations from the values of ε.

However, as argued above in section 5.2.e, RT quadrupole splittings are almost the same for all of the Ottawa samples. This is clearly seen in Fig.5.2.10 in which quadrupole splittings for both RT and LT are plotted as functions of sample purity. As explained in section 5.2.e, this implies that $\eta \propto 0$ in all the Ottawa samples and that at RT $\theta \propto \pi/2$ (PBH-like WF state) for essentially all the

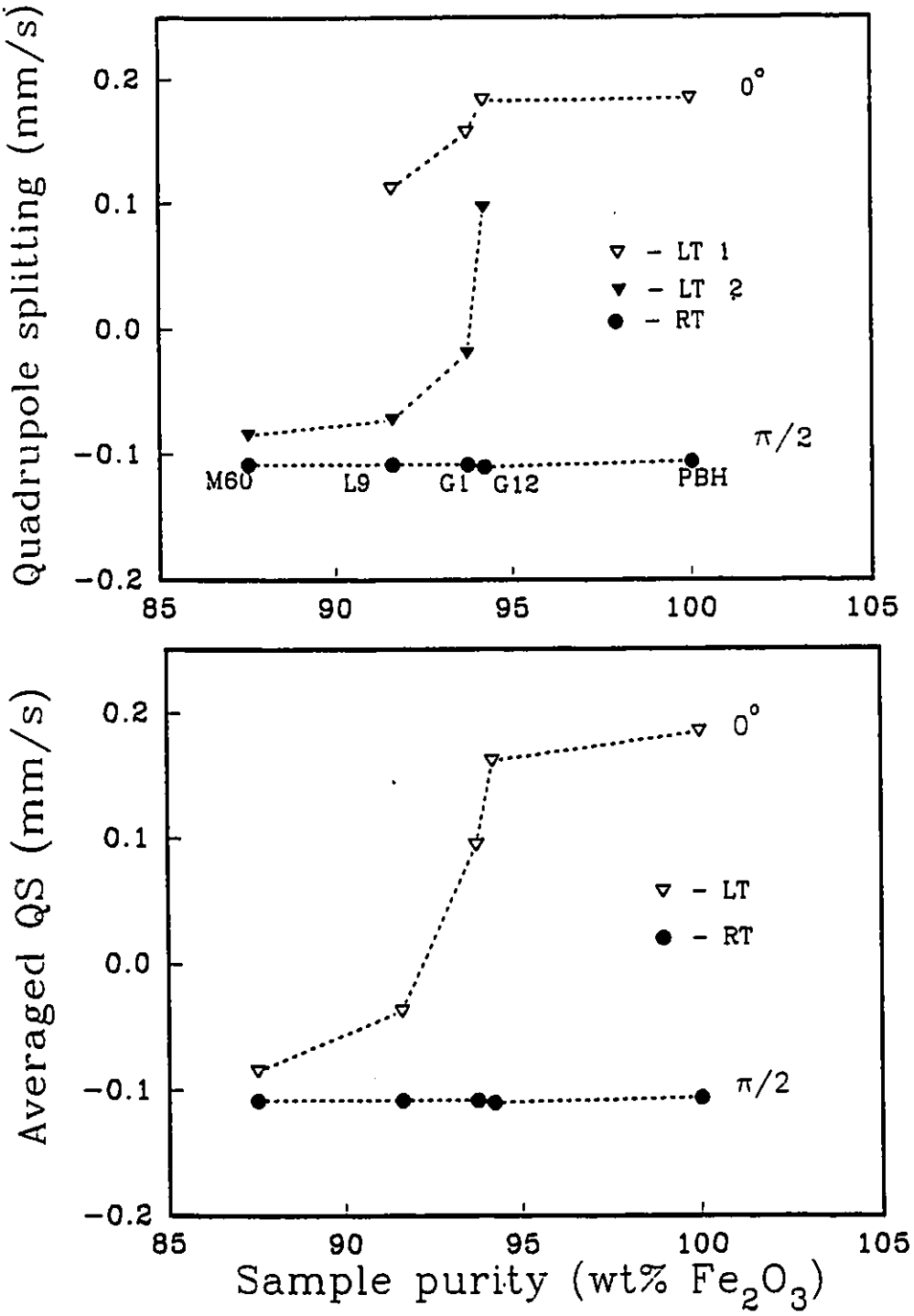

Fig 5.2.10 Quadrupole splittings for both RT and LT as functions of corrected (Table 5.1.1) sample purity. (top) For the two LT states and the RT state. (bottom) LT average and RT quadrupole splittings.

spins in each sample.

The fact that $\eta \simeq 0$ means that an effective mean value of θ can be taken to represent the mean value of ε. In particular at LT intermediate values of ε (between the PBH AF and WF values) are measured. We call the corresponding θ's effective θ's to emphases that actually the spins in a given non-PBH sample cannot all point exactly in one direction. This derived effective θ is only a quantity corresponding to a certain value of ε, via Eq.5.2.1 with $\eta = 0$. Nonetheless we can take it as an average spin direction. It is in this sense that most of the spins in all of the samples at RT align in the (111) direction.

Another important result given by Fig.5.2.10 is that at LT, quadrupole splittings change systematically from sample to sample. The difference between RT and LT states decreases with decreasing sample purity. In PBH the quadrupole splitting has a sharp change from -0.106 to 0.186 mm/s, changing sign and doubling its magnitude. This exactly corresponds to the Morin transition spin flip. From RT to LT, the iron spins flip from the basal plane (111) to the [111] direction, all of the iron in PBH participate in the Morin transition.

In our hematites G12, G1, L9 and M60, the quadrupole splittings at LT decrease significantly in the sequence of the sample purity. This is clearly shown in Fig.5.2.10.

The quadrupole splittings for both the PBH-like and defect states are drawn in Fig.5.2.10(a) and the averaged QS's over the two states are shown in Fig.5.2.10(b). We observe that the decrease of the quadrupole splitting is significant not only in the defect WF-like state, but also in the PBH-like AF state.

The different LT quadrupole splittings suggest that the spin orientations are different from sample to sample at LT. Then we can conclude that the spins reorient differently in different samples on going from RT to LT. At low temperature ($T << T_M(PBH)$), only in PBH are the spins parallel to the [111] direction. Otherwise, defects seem to stabilize moments that are more in the (111) plane.

Two phase coexistence was observed in many cases such as in hematites with Al-substitution (De Grave et al 1990), in hematites with different crystallinities (Chadwick et al.,1986), and in the hematites with various surface fractions (Van der Kraan, 1973, Nikolov et al., 1988). Moreover, the gradual spin rotation behavior at LT was reported by a neutron diffraction study on the $(1-x)\alpha Fe_2O_3-xAl_2O_3$ system (Kren et al., 1974). They found that the magnitude of the spin flipping gradually decreases with increasing x. When $x > 0.09$ the Morin transition did not occur.

Our results are in good agreement with the studies

above. All careful Mössbauer studies see two-phase coexistence at low temperatures in various non-PBH hematites. Both the Mössbauer studies and the neutron study can interpret their data in terms of an effective average θ that is found to have various intermediate values between the PBH values of 0 and $\pi/2$ that depend systematically on both temperature and known sample characteristics. We stress however that, in such non-PBH samples, the extracted θ's are <u>effective average θ's</u> in the sense explained above and that, in such samples, one should not expect all the spins (in the sample in either phase) to have a common direction defined by θ. De Bakker P M A et al (1990) have shown this elegantly by extracting distributions of θ from applied field Mössbauer measurements.

6. CONCLUSION

Our main conclusions can be stated as follows:

1. The sulphur measured by chemical analysis is probably completely contained in detected impurities such as $FeSO_4.OH$ and $Fe_2(SO_4)_3.nH_2O$ with $n \simeq 9\text{-}11$. It probably does not incorporate into the hematite at all, although the impurities may be closely associated to the hematite phase.

2. All of the Mössauer characteristics can be understood in terms of intra-hematite "defects" (i.e. surfaces and/or vacancies). The density of these defects is correlated to both the crystal quality of the hematite seen by XRD and the net hematite content (wt% Fe_2O_3) of the sample measured by chemical analysis. These correlations arise because the particular synthesis conditions cause both the hematite quality and the net hematite yield. No obvious correlations exist with the sample morphology seen by scanning electron microscopy.

3. Given the above noted correlations, either the hematite content or "sample purity" (wt% Fe_2O_3) or the total impurity content (100% - wt% Fe_2O_3) can be used to examine

the interrelations of the various Mössbauer characteristics.

At room temperature, the Mössbauer parameters that vary systematically with wt% Fe_2O_3 and that are therefore correlated to each other are:

—— the line widths and positions.

—— the average hyperfine fields.

—— the HFD widths.

—— the relative amounts of PBH-like material and higher defect density hematite.

At LT (T ≈ 80 K) the key Mössbauer parameters that correlate to wt% Fe_2O_3 are:

—— the relative amounts of hematite that has and has not undergone a Morin spin flip transition.

—— the average QS parameters ε that is related (via Eq.5.2.1) to an average effective spin rotation angle θ.

4. The higher defect hematite material seen in the RT spectra is preferentially the same material that at T ≈ 80K has not undergone a Morin transition, however, past some critical defect amount even that PBH-like material in such a sample does not undergo a Morin transition. For example, none of the hematite in sample M60 undergoes a Morin transition.

Finally, in ongoing work we have studied the effect of annealing sample M60 at various high temperatures in air and in vacuum. The annealed products have high quality hematite that undergoes a Morin transition. This and the fact that significant weight loss occurs at relatively low annealing temperatures support our conclusion #1.

In collaboration with Prof. G. Lamarche, we also measured the SQUID magnetometry of the Ottawa samples. These measurements corroborated our conclusions concerning coexistence of hematite materials that have and have not undergone Morin transitions at $T \simeq 80$ K.

REFERENCES

Artman J.O., Murphy J.C., Foner S. (1965)

Magnetic anisotropy in antiferromagnetic corundum-type sesquioxides.

Phys. Rev., Vol.138, 3A:912-917, 1965

Chadiwck J., Jones D.H., Thomas M.F., Tatlock G.J. and Devenish R.W.(1986)

A Mössbauer study of magnetic relaxiation and the Morin transition in amorphous and crystalline iron oxide systems. J. Magn. Magn. Mater., 59:301-308, 1986

De Grave E., Chambaere D., Bowen L.H.(1983)

Nature of the Morin transition in Al-substituted hematite. J. Magn. Magn. Mater., 30:349-354, 1983

De Grave E., Bowen L.H., Vochten R., Vanderberghe R.E.(1988)

The effect of crystallinity and Al substitution on the magnetic structure and Morin transition in hematite. J. Magn. Magn. Mater., 72:141-151, 1988

De Grave E., Vanderberghe R.E.(1990)

Mössbauer effect study of spin structure in natural hematites. Phys. Chem. Minerals, 17:344-352, 1990

Dutrizac J.E. (1989)

THE HYDROTHERMOAL CONVERSION OF JAROSITE-TYPE COMPOUNDS TO HEMATITE, in Productivity and Technology in the Metallurigical Industries, ed. Koch M, and

Tylor J.C., The Minerals, Metals & Materials Society, p.587-612, 1989

Dzyaloshinsky I. (1958)
A thermodynamic theory of "weak" ferromagnetism of antiferromagnetics.
J. Phys. Chem. Solids, 4:241-255, 1958

Gangas N.H.J., Bakas T.,Moukarika A.(1985)
Mössbauer study of the Morin transition.
Hyperfine Interaction, 23:245-258, 1985

Greenwood N.N., Gibb T.C. (1971)
Mössbauer spectroscopy (Chapman and Hall Ltd, 1971) p.47-66

Guinier A. (1963)
X-Ray Diffraction in Crystals, Imperfect Crystals, and Amorphous Bodies (Freeman W.H. and Company, 1963) p.124

Jiang J.S. Yang X.L. Chen L.W. and Zhou N.F. (1988)
A Mössbauer study on the surface hyperfine field of uniform hematite particles.
Appl. Phys., A45:245-247, 1988

Johnson C.E. Ridout M.S. and Cranshaw T.E. (1963)
Proc. Phys. Soc., 81:1079-1090, 1963

Kren E. Molnar B. Svab E., Zsoldos E.(1974)
Neutron diffraction study of the $(1-x)\alpha Fe_2O_3-xAl_2O_3$ system. Solid State Commun., 15:1707-1710, 1974

Kündig W., Bömmel H., Constabaris G., Lindqqist R.H. (1966)
Some properties of supported small α-Fe_2O_3 particales determined with the Mössbauer effect.
Phys. Rev., 142:327-333, 1966

Morin F.J. (1950)
Magnetic susceptibility of αFe_2O_3 and αFe_2O_3 with added Titanium. Phys. Rev., 78:819-820, 1950

Moriya T. (1963)
Weak Ferromagnetism, In Rado G.T. Suhl H. (eds.) Magnetism, Vol.1, Academic Press, New York, p.85-125

Morup S. Morten B.M. and Franck J. (1983)
A new interpretation of Mössbauer spectra of microcrystalline gpethite:"super-ferromagnetism" or "super-spin-glass" behaviour?
J. Magn. Magn. Mater., 40:163-174, 1983

Muench G.J., Arajs S., Matijevic E. (1985)
The Morin transition in small α-Fe_2O_3 particles.
Phys. Stat. Sol., 92:187-192, 1985

Murad E. and Johnston J.H. (1987)
Iron Oxides and Oxyhydroxides, in G.J. Long ed.: Mössbauer spectroscopy applied to inorganic chemistry (Plenum Publishing Corperation, 1987) Vol.2, p.507-582

Murad E. and Schwertmann U. (1986)
Influence of Al substitution and crystal size on the room-temperature Mössbauer spectrum of hematite.
Clays and Clay Minerals, Vol.34, 1:1-6, 1986

Nikolov O., Ruskov T., Tomov T. (1988)

A Mössbauer study of the Morin transition on the surface and in the bulk of hematite single crystals. Hyperfine Interaction, 39:409-417, 1988

Nininger R., Shroeer D. (1978)

Mössbauerstudies of the Morin transition in bulk and microcrystalline α-Fe_2O_3.

J. Phys. Chem. Solids, 39:137-144, 1978

Pankhurst Q.A.,Johnson C.E., Thomas M.F. (1986)

Mössbauer measurements of the spin-flop transition in some α-Fe_2O_3 crystals.

J. Magn. Magn. Mater., 54-57:1163-1164, 1986

Ping J.Y. and Rancourt D.G. (1992)

Physical basis and break down of hyperfine field distribution analysis in fcc Fe-Ni (5-70 at%Fe).

J. Magn. Magn. Mater., 103:285-313, 1992

Rancourt D.G. (1981)

A Mössbauer study of the paramagnetic-antiferromagnetic alloy $Fe_{2-x}Cr_xAs$. M.S. thesis. University of Toronto

Rancourt D.G. and Ping J.Y. (1991)

Voigt-based methods for arbitrary-shape static hyperfine parameter distributions in Mössbauer spectroscopy. Nucl. Instr. and Meth., B58:85-97, 1991

Rancourt D.G. Julian S.R. and Daniels J.M. (1985a)
Mössbauer characterization of very small superparamagnetic particles; application to intra-zeolltic α-Fe_2O_3 particles.
J. Magn. Magn. Mater., 49:305-316, 1985

Rancourt D.G. Daniels J.M. and Lam H.Y. (1985b)
A ^{57}Fe Mössbauer study of Fe_2As: a magnetically induced electric-field-gradient asymmetry
Can. J. Phys. Vol.63, 12:1540-1547, 1985

Schroeer D. and Niniger R.C. (1967)
Morin transition in α-Fe_2O_3 microcrystals
Phys. Rev., Vol.19, 11:632-634, 1967

Van der Woude F. (1966).
Mössbauer effect in α-Fe_2O_3
Phys. Stat. Sol., 17:417-432, 1966

Van der Kraan A.M. (1973)
Mössbauer effect studies of surface ions of ultrafine α-Fe_2O_3 particles.
Phys. Stat. Sol., 18:215-226, 1973

Vandenberghe R E (1990)
An improved, two-parameter distribution method for the description of the Mössbauer spectra of magnetic small particles in an applied field.
Meas. Sci. Technol., 1:954-964, 1990

Verbeeck A.E., De Grave E and Vandenberghe R.E.(1986)

The effect of the particle morphology on the Mössbauer effect in α-Fe_2O_3.

Hyperfine Interaction, 28:639-642, 1986

Waychunas G.A. (1991)

Crystal Chemistry of Oxides and Oxyhydroides, in Lindsley D.H. ed., Oxide Minerals, Vol.25, p.11-68